

1

2 **Projected Hydroclimate Changes Driven by Carbon Dioxide Trends and Vegetation**
3 **Modeling in CMIP6**

4 **Paul A. Dirmeyer^{1,2}, Kai Huang², Nikki Lydeen², Zachary Manthos², Scott Knapp² and**
5 **Finley Miles Hay-Chapman²**

6

7 ¹Center for Ocean-Land-Atmosphere Studies, George Mason University, Fairfax, Virginia, USA.

8 ²Department of Atmospheric, Oceanic and Earth Sciences, George Mason University, Fairfax,
9 Virginia, USA.

10

11

12

13 Corresponding author: Paul A. Dirmeyer (pdirmeye@gmu.edu)

14

15

16

17

18

19

20 **Key Points:**

- 21 • Factors other than increasing atmospheric CO₂ contribute markedly to changes in
22 hydroclimate across much of the globe
- 23 • Accounting for interannual terrestrial water storage provides a more accurate relationship
24 between evaporation, precipitation and aridity
- 25 • Hydroclimate response to increasing CO₂ significantly depends on the treatment of
26 vegetation in Earth system models

27

28 Abstract

29 Past and projected changes in global hydroclimate in Earth system models have been examined.
30 The Budyko framework that relates the partitioning of precipitation into evaporation to a
31 location's aridity has been modified to account for the effect of interannual terrestrial water
32 storage and compared to traditional methods. The new formulation better fits climate model data
33 over most of the globe. Old and new formulations are used to quantify changes in the spatial
34 patterns of hydroclimate based locally on year-to-year variations water and energy cycle
35 variables. Focus is on multi-model median responses to changing climate. The changes in
36 hydroclimate from preindustrial to recent historical (1965-2014) conditions often have different
37 patterns and characteristics than changes due only to increasing CO₂. For simulations with
38 gradually increasing CO₂, differing model treatments of vegetation are found specifically to have
39 categorically different impacts on hydroclimate, particularly altering the relationship between
40 aridity and the fraction of precipitation contributing to evaporation in models that predict
41 vegetation changes. Models that predict vegetation phenology have consistently different
42 responses to increasing CO₂ than models that do not. Dynamic vegetation models show more
43 widespread but less consistent differences than other models, perhaps reflecting their less mature
44 state. Nevertheless, there is clearly sensitivity to vegetation that illustrates the importance of
45 including the representation of biospheric shifts in Earth system models.

46

47 Plain Language Summary

48 "Hydroclimate" means aspects of climate related to the water cycle, like the fraction of
49 precipitation that evaporates back into the atmosphere (evaporation ratio), or how dry a location
50 is (aridity). Such hydroclimate parameters are not independent of one another: evaporation ratio
51 and aridity are strongly coupled via the Budyko relationship, with consequences for water
52 resources, groundwater recharge, river flows and vegetation health. The Budyko relationship
53 itself varies spatially due to climate, soil properties, terrain and vegetation. Hydroclimate
54 changes in a changing climate, but vegetation adds an extra layer of complexity. We find that
55 hydroclimate changes from only CO₂ increases do not resemble historical changes in a large
56 suite of climate models, due to added effects from vegetation as well as aerosols and other
57 climate forcings. As CO₂ increases, models that predict seasonal to interannual fluctuations in
58 vegetation phenology (greenness, canopy density, etc.) have consistently different responses than
59 simpler models that do not. Models that also predict the extinction and migration of biomes show
60 even more widespread but less consistent differences in the evolution of hydroclimate. Careful
61 consideration needs to be given to the role vegetation plays in hydroclimate, as water resources
62 will not only be affected by future warming.

63

64 **1 Introduction**

65 Over periods of at least one year (i.e., neglecting the seasonal cycle), fluctuations in the
 66 storage of water below the land surface are generally small relative to the fluxes inward
 67 (precipitation) and outward (evapotranspiration and runoff). The same is true for heat, where the
 68 primary input is absorbed solar radiation, and outputs are net longwave radiation and turbulent
 69 heat fluxes. These two quasi-equilibrium budgets are linked, in that energy that escapes the land
 70 surface as turbulent latent heat flux is the energy used to remove water from the land in the form
 71 of evapotranspiration (E) into the atmosphere. The functional relationship between E ,
 72 precipitation and net radiation derived by Budyko (1974) has the essential characteristics that in
 73 arid regions $R_{net}/\lambda P \gg 1$, where R_{net} is average net radiation, P is average precipitation and λ
 74 is the latent heat of evaporation. A consequence is that nearly all precipitation is lost to land as
 75 evaporation in arid regions. In humid regions where $R_{net}/\lambda P \ll 1$, E approaches its potential
 76 rate, which is limited by lack of available energy.

77 The quasi-equilibrium Budyko perspective is thus built around these two limits: energy
 78 limitations on E in humid regions and moisture limitations on E in arid regions (Sposito, 2017).
 79 Lacking any temporal variability in precipitation or net radiation, a location having $R_{net} = \lambda P$
 80 might be expected to experience no limitations on E . In reality this is not the case. Locations
 81 where long-term $R_{net}/\lambda P \cong 1$ are often locations that experience a seasonal cycle that oscillates
 82 between energy and moisture limitations on E , experiencing a wet season with significant runoff
 83 and a dry season when soil moisture declines toward the wilting point. As a result, long term
 84 rates of E can be well below the limits suggested by either energy or moisture limitations (Milley,
 85 1994). Storage of water below the land surface can moderate this seasonality, extending the
 86 hydrologic time scale and supplying more water for E and runoff during the dry season than
 87 contemporaneous precipitation would allow. Yet other physical restrictions also limit E , such as
 88 the finite depth of plant roots and plant physiological responses to environmental stresses within
 89 the diurnal cycle (Ye et al., 2015).

90 The assumptions and limits inherent in the Budyko relationship underpin much of the
 91 theory of land-atmosphere (L-A) interactions (Santanello et al., 2018). Namely, soil moisture can
 92 act as a regulator of surface heat fluxes, controlling the partitioning of net radiation between
 93 latent and sensible heat flux (and thus the rate of E) at places and times when net radiation is
 94 abundant. Otherwise, the available energy from net radiation is itself the controlling factor on E .
 95 Concomitant modulation of sensible heat fluxes affects boundary layer development in the lower
 96 troposphere, with consequences for atmospheric thermodynamics, convective cloud formation,
 97 and the general circulation (Betts, 2004).

98 Applications of the Budyko model in the phase-space portrayed by the evaporation ratio
 99 (or E ratio: E/P) as a function of aridity ($R_{net}/\lambda P$) fall into three categories. First is the local
 100 climatological application at one or more specific locations. A single location may be a flux
 101 tower where the three essential quantities P , E , and R_{net} are measured directly, a hydrologic
 102 catchment where at least P and perhaps R_{net} are measured but E is inferred from P and
 103 streamflow measurements at the exit of the catchment, or a grid cell from a climate model or
 104 ecohydrologic model. In this case, data are gathered over many years to determine a single point
 105 for the values of aridity versus E ratio space, which provides a two-parameter definition of that
 106 location's hydroclimate (Destouni et al., 2013; Oudin et al., 2008; D. Wang & Tang, 2014; L.
 107 Zhang et al., 2004).

108 The second category is a variation of the first, wherein *interannual* variations in E ratio
 109 versus aridity space are charted to determine the hydroclimatic variability of the location over
 110 time, typically applied at an annual time step hydroclimate (Jiang et al., 2015; R. D. Koster &
 111 Suarez, 1999; Ning et al., 2019; D. Yang et al., 2009; Hui Yang et al., 2018; Ye et al., 2015). If
 112 variations are normally distributed, means and standard deviations can provide sufficient
 113 information to characterize hydroclimatic variability in time. But frequently the time distribution
 114 of these parameters is not normal, especially for the aridity index in dry regions, which can
 115 become extremely large in drought years. Medians and quartiles provide a more robust
 116 characterization of such variability.

117 In the third category, the first approach is applied over many locations, and the
 118 climatological values plotted to portray the *spatial* variations of E ratio versus aridity (Carmona
 119 et al., 2016; Dirmeyer & Zeng, 1999; Greve et al., 2020; Li et al., 2018; Miralles et al., 2016;
 120 Porada et al., 2011; Xu et al., 2013). This also allows maps of aridity and E ratio to be produced
 121 (Kumar et al., 2016; Zhou et al., 2015). Furthermore, the direct relationships between other water
 122 and energy balance terms to the central Budyko variables allow for other useful applications
 123 (e.g., Koster 2015; Roderick and Farquhar 2011; Brubaker et al. 1993; Burde and Zangvil 2001).

124 The result of either categories 2 or 3 is a distribution of points in the ($R_{net}/\lambda P$, E/P)
 125 plane. Many physically motivated but ultimately empirical functions have been derived to fit the
 126 distribution of points as if E/P were a monotonic function of $R_{net}/\lambda P$. Budyko's original
 127 formulation took the form:

$$\frac{E}{P} = \left[\frac{R_{net}}{\lambda P} \left(1 - e^{-R_{net}/\lambda P} \right) \tanh \left(\frac{\lambda P}{R_{net}} \right) \right]^{1/\omega_B}, \quad \omega_B = 2.0$$

128 where the exponent ω_B was a fixed number. Subsequently, many formulations have been
 129 proposed in order to provide flexibility to optimize the fitting of the function to data (cf. Yang
 130 and Yang 2011). One popular formation is that of Fu as described by Zhang et al. (2004):

$$\frac{E}{P} = 1 + \frac{R_{net}}{\lambda P} - \left[1 + \left(\frac{R_{net}}{\lambda P} \right)^{\omega_F} \right]^{1/\omega_F}$$

131 where ω_F is a tunable parameter that implicitly represents hydrologic characteristics of
 132 the location, such as subsurface water storage capacity and seasonality in aridity. Most such
 133 tunable formulations of the Budyko relationship rely on a single parameter. Given the
 134 assumptions that the function converges asymptotically to the energy and water limits at low and
 135 high aridity respectively, the single parameter controls how closely the function conforms to the
 136 limits in the neighborhood of $R_{net}/\lambda P \sim 1$. A number of variations on the single parameter
 137 Budyko formulation have been proposed (e.g., Choudhury 1999; Zhang et al. 2001, 2004; Wang
 138 and Tang 2014) with the goal of better fitting the relationship to observed data for various
 139 applications.

140 As the tuning parameter effectively moves the fitted curve closer or farther from the
 141 limits described above, the parameter itself becomes an index of the hydroclimatology described
 142 by annual mean fields of precipitation, ET and net radiation at a given location. In a changing
 143 climate, wherein assumptions of hydrologic stationarity are violated (Milly et al., 2008, 2015),
 144 there is no reason to assume that the hydroclimatological distributions described by the Budyko
 145 relationship should not change as well. Previous studies have examined this using climate model

146 simulations from the fifth Climate Model Intercomparison Project (CMIP5; Taylor et al. 2012) to
 147 quantify future hydrologic sensitivity (Kumar et al., 2016; Singh & Kumar, 2015), spatial
 148 hydroclimate variability (category 3 above; Li et al. 2018), and projected runoff changes (Milly
 149 & Dunne, 2016; Osborne & Lambert, 2018; Zheng et al., 2018). However, application of the
 150 parameter itself as an index of hydroclimatic change has been limited. Yang et al. (2018)
 151 recognized the application of such an index as an indicator of the water retention characteristics
 152 at the catchment scale, as well as noting the potential influence of vegetation responses to
 153 increasing CO₂ and temperature as a factor in its change. In fact, many different possible
 154 influences are agglomerated into such a single parameter.

155 In this study, we examine the use of such a hydroclimatic index taken as a single
 156 parameter from various formulations of the Budyko relationship as an integrative indicator of
 157 climate change impacts on the hydrologic cycle. Using data from CMIP6 (Eyring et al., 2016),
 158 we examine how the hydroclimatological position and interannual variability in Budyko space of
 159 any location may change from past to present and as a result of ever-increasing greenhouse gas
 160 concentrations in the atmosphere. We examine how well different climate models agree on the
 161 positions and spatial patterns of the hydroclimatic index estimated from a best fit to model data,
 162 using a curve-fitting procedure at each location through yearly values in Budyko space, and
 163 determine multi-model consensus estimates. Finally, we attempt to attribute changes in aridity, E
 164 ratio and the ω parameter to changes in CO₂ and vegetation.

165 The data used, models considered, and analysis methods are described in section 2.
 166 Results are shown in sections 3 and 4, showing first the variability of aridity and E ratio, then
 167 examining three formulations of the Budyko curve to synthesize hydroclimate impacts. The
 168 potential role of vegetation and its simulation in different Earth system models is examined in
 169 section 5, and a summary of results is presented in section 6.

170 2 Methodology and Data

171 2.1 Fitting of Budyko formulations

172 Using annual mean data calculated from the monthly output of 37 CMIP6 models (see
 173 Tables 1 and S1), we find median values and interquartile ranges (IQR) of both aridity and E
 174 ratio for every land grid cell on each models' native output grid for each of four periods taken
 175 from three DECK simulations described below. We also use the time series of annual values of
 176 aridity and E ratio to produce scatter plots in Budyko space through which several different
 177 single parameter formulations of the Budyko relationship are fit, using a basic least-squares
 178 difference minimization approach to find the optimum value of the ω parameter.

179 Several different formulations are explored. The Fu formulation described above has
 180 been used in this curve-fitting context in many previous studies and we use it here, estimating
 181 values of the parameter ω_F as a function of location for each model and experiment situation
 182 described below. We also use the original Budyko formulation but allow the parameter ω_B to
 183 vary so that it can be used for better fitting of the function.

184 Because of the extreme heteroscedasticity of data in Budyko space at many locations,
 185 obtaining a good fit to the data is challenging. That was a primary motivation for exploring more
 186 than one formulation. Furthermore, we have found that specific formulations tend to perform
 187 better in some climate regimes than others. Here we describe problems faced in applying the Fu

188 and modified Budyko formulations, and how that has led us to a novel formulation that appears
 189 to fit the range of data best. All three are used in our analyses and are ultimately compared.

190 As mentioned above, the classical Budyko relationship depicts evaporation ratio E/P as a
 191 function of aridity $R_{net}/(\lambda P)$. In this framework. Hydroclimatological limits suggest that for any
 192 period with a duration of an integer number of years ≥ 1 , $E/P \leq R_{net}/(\lambda P)$ for $R_{net}/(\lambda P) < 1$,
 193 and $E/P \leq 1$ for $R_{net}/(\lambda P) > 1$. For CMIP6 models, the first limit appears to be obeyed
 194 rather firmly but the second frequently is not. So, in all cases, points that exceed $E/P > 1.2$ are
 195 removed from the sample before parameter optimization. Also, over very dry locations,
 196 extremely large values of $R_{net}/(\lambda P)$ can result – often exceeding 100. Points at such high aridity
 197 can greatly impact the curve fitting, so all values of $R_{net}/\lambda P > 8$ are also removed from the
 198 sample. For purposes of representing the Budyko framework, it is the values of E ratio closer to
 199 $R_{net}/\lambda P \sim 1$, where the second derivative of fitting functions is largest, that provide the most
 200 information about the effects of soil water retention, vegetation, etc., on E – runoff partitioning
 201 (Kumar et al., 2016).

202 Some examples of fits through data at single points are shown in Figure 1. We find that
 203 the Fu formulation does very well in wet and moderate regions but struggles in arid locations. It
 204 appears that often the E ratio begins dropping at relatively high values of aridity, nor does it
 205 appear to asymptotically approach the $E/P = R_{net}/(\lambda P)$ limit in wetter situations. This may be
 206 due to a propensity for rainfall in such arid regions to come in infrequent but heavy downpours
 207 that contribute to large runoff, or easily permeate sandy soils becoming unavailable to
 208 evaporation. However, the Budyko formulation with a variable exponent ω_B attains something of
 209 a sigmoid shape for $\omega_B < 2$, which nicely adapts to the data distributions in arid locations.

210 Conversely, the variable exponent Budyko formulation struggles to fit data from humid
 211 regions, especially when there are frequently values of $E/P > 1$. The best fit is often attained for
 212 values of $\omega_B > 2$, wherein the fitted curve violates the energy-constrained limit $E/P \leq$
 213 $R_{net}/(\lambda P)$. These problems prompted a search for a new formulation that would work well in all
 214 climates.

215 We found that applying a moving average of 3 or 5 years lessened but did not remove
 216 instances of $E/P > 1$ for most models in most locations, yet removed variability, suppressed the
 217 tails in the distribution along the aridity axis, and reduced the number of degrees of freedom in
 218 the time series hampering statistical significance. Annual $E/P > 1$ is an indicator of substantial
 219 water storage, which is a hydrological characteristic of the system that should not be completely
 220 removed from consideration. Since years having $E/P > 1$ appear to be a common occurrence,
 221 we relaxed the constraint that the function must not exceed unity, although an asymptotic
 222 approach to unity is a clearly desirable characteristic for semiarid and arid climates. The best
 223 formulation we found was another slight variant on the original Budyko formula:

$$\frac{E}{P} = \frac{R_{net}}{\lambda P} \left(1 - e^{-R_{net}/\lambda P}\right) \tanh\left(\frac{\lambda P}{R_{net}}\right) \omega_Z$$

224 Here, the parameter ω_Z is a multiplicative factor rather than in an exponent. It retains the
 225 sigmoid at small aridity values, approaches the limit $E/P = 1$ for $\omega_Z \leq 1$, but is free to exceed
 226 that limit for $\omega_Z > 1$. Example results for this Budyko formulation without the E/P constraint
 227 are shown in the bottom row of Figure 1.

228 2.2 CMIP6 model data

229 We use output from three of the DECK experiments: piControl, historical, and 1pctCO2.
 230 However, there are four distinct periods and situations for which indices are calculated:

- 231 1. All years from piControl (~600 years): PI
- 232 2. The last 50 years of historical, representing late 20th and very early 21st century
 conditions): H_{L50}
- 233 3. Years 21-70 of 1pctCO2, which will lie in the range of 21st century CO2 levels, out to
 circa 2070 based on current projections: $1\%_{21-70}$
- 234 4. Years 91-140 of 1pctCO2, which approach the 4xCO2 levels, representing the first half
 of the 22nd century if little is done to ameliorate emissions: $1\%_{91-140}$

235 The historical simulation differs from the others in that it includes not only greenhouse
 236 gas forcings, but also observed land use changes, detailed trends in volcanic and anthropogenic
 237 aerosols, trace atmospheric constituents and solar forcing. With these four temporal samples,
 238 differences found between specific pairs are indicative of specific changes and sensitivities in the
 239 hydroclimate at locations for the various models. Specifically, we consider several pairings that
 240 address the following questions:

- 241 1. How has the hydroclimate changed since pre-industrial times [$H_{L50} - PI$]?
- 242 2. How is hydroclimate affected by a steady increase in atmospheric CO₂ to an approximate
 doubling [$1\%_{21-70} - PI$]?
- 243 3. How might hydroclimate change from a doubling to a quadrupling of atmospheric CO₂
 [$1\%_{91-140} - 1\%_{21-70}$]?

244 To keep all models on equal footing, only one ensemble member from each model is
 245 included (r1i1p1f1, unless that member is not available, in which case the next lowest variant
 246 that is available for all variables in an experiment is used – see Table 1 for details). Past results
 247 with CMIP5 suggest such indices are rather robust within experiments and not sensitive to the
 248 choice of ensemble member, nor the use of all members, when compared to differences between
 249 experiments or between models. Furthermore, the majority of the experiments for the models
 250 only provide a single simulation, so this choice puts all models on an equal footing regarding
 251 sample size.

252 Most models predict intraseasonal, seasonal and interannual variations in vegetation
 253 coverage and greenness, referred to as vegetation phenology. Several include a dynamic
 254 vegetation model (DVM) that can simulate the multi-year evolution and migration of biomes in
 255 response to climate changes (see supplemental Table S1). Not all the models' treatments of
 256 vegetation could be determined, as discussed in section 5.

257 At the time of analysis, 37 models provided the monthly mean data required to depict the
 258 three necessary quantities for describing model hydroclimatology in Budyko space, namely total
 259 precipitation (CMIP variable: pr), total evaporation (expressed as a latent heat flux: hfls) and net
 260 radiation (estimated as the sum of hfls and sensible heat flux: hfss). Note that in several
 261

266 instances, more than one version of a model from the same institution is included. It can be
 267 debated whether, in multi-model analyses, each model should be given equal weight or rather
 268 each institution, as there is often great similarity between results from related models. We note
 269 that the models used by many institutions are themselves descended from a small number of
 270 pioneering Earth system modeling efforts. Thus, the genetic differences, so to speak, among
 271 models are not simply discerned by the institution names listed here. We present multi-panel
 272 depictions of results from all models in the supplemental material for visual comparison, so the
 273 reader can judge the degrees of diversity represented among model results.

274 2.3 Multi-model analysis

275 In order to perform direct comparisons and produce multi-model statistics, median and
 276 IQR of aridity, E ratio, and estimates of ω_B , ω_F and ω_Z are interpolated to a common high-
 277 resolution longitude by Gaussian latitude grid (2560 x 1280 grid cells) to preserve the spatial
 278 detail and coastlines of each model (Dirmeyer et al., 2013b). A nearest-neighbor interpolation is
 279 used for each model including only land grid cells from each model; at least 90% of the models
 280 must project an ice-free land cell into each high-resolution grid cell for the value to be retained –
 281 otherwise it is assumed to be an open water or ice covered point and is masked.

282 Multi-model statistics are mainly based on medians to prevent outlier models from overly
 283 affecting the multi-model result. When examining the changes in the five file pairings described
 284 above, three approaches have been examined at each grid cell. The simple change in the multi-
 285 model median has been considered but found to be rather noisy. The median of the 37 changes in
 286 the individual models is found to give a more robust depiction of changes. Finally, the method of
 287 Dirmeyer et al. (2013a,b) has been used to determine the number of models showing a change of
 288 a particular sign, regardless of magnitude, and the significance of the distribution. The null
 289 hypothesis for the final method is that the change projected by each model is a random fair coin
 290 toss. Each possible split $n : 37 - n$ has an associated probability of occurring by chance, which
 291 provides a significance of consensus that complements the changes in medians used to quantify
 292 the magnitudes of changes.

293 3 Aridity and Evaporation Ratio

294 Before investigating the Budyko curve estimations, we first examine the climatologies
 295 of aridity and E ratio. Figure 2 shows, for the PI experiment, the multi-model median of these
 296 two quantities, along with the inter-model standard deviation and the normalized difference
 297 between the mean and median. The last quantity is an indication of skewness in the distribution
 298 across models. Given that the Budyko relationship describes a monotonic relationship between
 299 aridity and E ratio, it is no surprise that the maps of their medians are very similar. Humid
 300 regions have low values of both aridity and E ratio and dry regions have high values. Semi-
 301 humid to semi-arid transition regions tend to have high values of E ratio but relatively moderate
 302 aridity, reflecting the classical shape of the Budyko curve. Figures S1 and S2 show the temporal
 303 medians for each model – the multi-model statistics are calculated from the individual model
 304 medians.

305 The pattern of standard deviation of these quantities among models in Figure 2 largely
 306 mirrors their magnitudes. The difference between multi-model mean and median, normalized by
 307 standard deviation, shows some interesting patterns. For aridity this quantity is predominantly
 308 positive, indicating a positive skewness, i.e., there are a few models that tend towards very large

values of aridity. This is especially strong over the desert regions of North Africa and Asia, but also over much of India, regions in and around the Andes, and relatively semi-arid regions surrounding the Ethiopian highlands. For E ratio, weak negative values cover most land areas, suggesting a negative skewness in the distribution across models. The notable exception is across the core of the Sahara where strong positive skewness extends. There are also areas of strong positive values along coastal margins of deserts, which could reflect large variations among models' quantification of dew and its evaporation where oceanic winds carry humid air over arid coastlines. However, these may also be an artifact of model treatments of coastal points or inaccuracies in our determination of land-sea masks for some models that did not supply such information, we cannot rule out that oceanic evaporation for some models may be counted as terrestrial. The investigation of skewness of the distributions provides another reason to focus on medians throughout this study.

Figure 3 depicts the year-to-year variability in PI for the aridity and E ratio at each location, again shown in terms of multi-model median, inter-model standard deviation and the normalized difference between the mean and median. The quantity used is inter-quartile range (IQR) – the difference between the 75th and 25th percentile in the distribution of all annual values across all years of the piControl simulation for each model. The spatial pattern of the multi-model median of IQR for aridity closely resembles the median and standard deviation from Figure 2, but the IQR for E ratio is rather different. Whereas aridity IQR appears large across all arid regions, for E ratio it is largest around upper Egypt and lands surrounding the Persian Gulf and Arabian Sea. Most arid regions have relatively modest IQR for E ratio, on par with semi-arid and humid regions.

Inter-model standard deviation for IQR is again highest in arid regions, but more limited in extent for E ratio. India is again an area of pronounced disagreement among models, given that much of it is not arid. Model agreement is high for both quantities in tropical rainforest areas, west-central China, the Canadian Rockies, Quebec and Scandinavia. Skewness tends to be large and positive over many areas for aridity IQR over arid and semi-arid regions, but also mountainous and coastal regions of South America, yet generally low over North America and Europe. For the IQR of E ratio, skewness in the model distribution is large and positive over the Sahara, southeastern Arabia, the coasts of southwestern Asia including the Indus valley, and the Tarim Basin.

Changes from past to present and for different intervals along the 1pctCO₂ experiment for aridity and E ratio are shown in Figures 4 and 5 respectively. Changes are displayed in two ways – as the median of changes among all models, and as the fraction of models displaying a positive or negative change, colored by the likelihood of such a distribution occurring by chance. The latter gives a clear indication of significance of agreement among models, while the former conveys information about the magnitude of the change.

Aridity changes are large but often rather meaningless over the interior of North Africa and Arabia, given the very large medians and standard deviations there already; strong coloring in the bottom panels suggest where changes may be consequential. For instance, ongoing increases in aridity along the coastal regions of North Africa and the Mediterranean appear to be significant.

For H_{L50} – PI there are generally decreases in aridity and accompanying E ratio over large areas of the Northern Hemisphere that include forest regions in North America and Eurasia,

and areas that experienced expanded agriculture: much of the Indian subcontinent, eastern China, central North America, and much of central and eastern Europe extending east across the Eurasian steppes. The decrease in aridity is especially strong in magnitude over the upper Indus Basin, but that region, like much of the Indian subcontinent, mainly sees an increase in E ratio, possibly due to the increased irrigation being correctly represented in many of the climate models. At lower latitudes, there is strong consensus for a decrease in aridity over much of tropical Africa, the Pampas of South America and Uruguay, as well as parts of western Australia. E ratio also decreases over the Nordeste region of Brazil, but increases over the eastern Amazon Basin, the Orinoco Basin, and across much of the subtropics.

The trends in the two intervals of the 1pctCO₂ case, 1%₂₁₋₇₀ – PI (middle columns of Figures 4 and 5) and 1%₉₁₋₁₄₀ – 1%₂₁₋₇₀ (right columns of Figures 4 and 5), resemble each other with the main difference being changes in the later interval are generally stronger. Some of these features are seen in H_{L50} – PI as well, but some are not. For instance, the broad areas of decreasing aridity and E ratio over much of North America, Eurasia and central Australia in H_{L50} – PI reverse to increases in 1%₂₁₋₇₀ – PI. All three show decreasing aridity over the Indus Valley, although there is great variability in model agreement patterns over South Asia among intervals. All show decreasing aridity and E ratio over central Africa. Aridity also decreases over much of China, Patagonia and the Pampas, while E ratio decreases over the Nordeste. All show increasing aridity and E ratio over Mesoamerica, northern South America, the Mediterranean and much of southern Africa.

For the two intervals that represent pathways of a changing climate from preindustrial conditions, we see some similarities that may be attributable to comparable increases in atmospheric CO₂. The CO₂ concentration in 1%₂₁₋₇₀ is greater than in H_{L50}, averaging 447.2 ppm in the 50-year period versus 354.2 ppm in H_{L50}, and indeed the common features are generally stronger for 1%₂₁₋₇₀ – PI than for H_{L50} – PI. The different features noted may be due to the additional forcings in the historical experiment – this is explored further in section 5.

4 Budyko Curves

Next, the spatial distributions of the shape of the three Budyko curves, specified by different one-parameter formulations, are investigated. There is not a one-to-one correspondence between the magnitude of the parameters ω_B , ω_F and ω_Z , so we emphasize the spatial patterns over their values. However, each has the same general characteristics such that for lower parameter values, the curve sits lower in Budyko-space, i.e., a lower value of E ratio for a given value of aridity. For high parameter values, the curve approaches $E/P = R_{net}/\lambda P$ when $R_{net}/\lambda P < 1$. For the variable exponent Budyko formulation and Fu formulation, large parameter values lead to $E/P \rightarrow 1$ when $R_{net}/\lambda P > 1$, but this limitation is not in place for the formulation without the upper limit on E/P (see Figure 1).

Figure 6 shows the multi-model median values of, from left to right, ω_B , ω_F and ω_Z , as well as the standard deviation among models of the median, and the skewness index described previously. All three formulations tend towards low values of ω over arid regions, and high values in tropical forests. Beyond that there are some stark differences. Outside the tropics, the Budyko formulation with the tunable exponent has the highest values of ω_B in transitional regions, not the most humid locations. The Fu formulation places the lowest values of ω_F in mountainous and Arctic locations, not in deserts. Some of the lowest values of ω_F are in extratropical rainforests. The Budyko formulation without the E/P constraint tends to resemble a

397 map of R/P in spatial pattern, where R is runoff. Interestingly, it also results in much smoother
 398 spatial patterns compared to the other formulations, and except for alpine and arctic climates it
 399 has much reduced inter-model variability (middle row of Figure 6). Estimates of ω_B and ω_F
 400 show global positive skewness (bottom row of Figure 6) whereas ω_Z shows a mix of positive and
 401 negative skewness, with pronounced negative skew over the Sahara and Arabia.

402 Figure 7 shows which of the three formulations has the best fit at each location,
 403 quantified as the lowest root mean square error (RMSE) of the curve through all yearly points in
 404 the Budyko space (E/P versus $R_{net}/\lambda P$). The RMSE maps for each formulation are shown in
 405 Figure S3. The Budyko formulation without the E/P constraint is the best formulation in the
 406 majority of locations, especially in the subtropics and areas that are not at either extreme (not
 407 very wet nor arid). The Budyko formulation with tunable exponent is generally most trustworthy
 408 in arid regions and a number of high-latitude locations. The Fu formulation is particularly good
 409 across northern Europe, some tropical regions, and a smattering of other locations. It should be
 410 noted that the Budyko formulation without the E/P constraint will necessarily have $\omega_Z \lesssim 1$ in
 411 locations where aridity $R_{net}/\lambda P > 1$ predominates and will have $\omega_Z > 1$ where $R_{net}/\lambda P < 1$
 412 even when $E/P < 1$ is always true. This is because the fitting of the function to the distribution
 413 of points is optimized in these situations.

414 Figure S4 gives a pairwise comparison of the multi-model median values of RMSE of the
 415 best fit for the three formulations in the Budyko-space (E/P versus $R_{net}/\lambda P$) as a set of three
 416 scatter diagrams for all land grid cells in the PI case. The coloring shows the median aridity of
 417 each grid cell; RMSE generally increases with aridity, as was also evident in Figure S3. The left
 418 panel compares the Fu formulation to the variable exponent Budyko formulation. There is little
 419 overall advantage of one formulation over the other, but the preponderance of dark blue points
 420 toward the upper left-hand corner illustrates how the Fu formulation struggles in some wet
 421 climates. It also tends to do slightly more poorly in fitting very dry climates (pink) but tends to
 422 be better in the semi-humid to semi-arid regime (green). The other two panels of Figure S4
 423 compare the new unconstrained Budyko formulation (y-axis) to the others. While the fit is
 424 generally a bit poorer in very humid regions, it tends to excel in all others except some very arid
 425 locations relative to the original Budyko formulation with the tunable exponent.

426 As a final measure of the goodness of fit of each of the formulations, Figure S5 shows the
 427 displacement of the multi-model median values of aridity and E ratio from the nearest point on
 428 the best fit Budyko curve using the multi-model median value of ω . Because of the nonlinear
 429 nature of the Budyko curves, there is no expectation that the means should fall on the curve, let
 430 alone the medians. Nevertheless, we see for all three formulations the displacement in Budyko
 431 space tends to be large in arid regions, moderate in semi-arid regions, and highly variable
 432 elsewhere.

433 Changes in the ω parameter between CMIP6 experiments for each formulation of the
 434 Budyko curve are shown in Figure 8. There are common features to each formulation: A broad
 435 reversal in changes between the Northern Hemisphere versus low latitudes and the Southern
 436 Hemisphere, and many regional features. As with aridity and E ratio, the global pattern of
 437 changes in $1\%_{91-140} - 1\%_{21-70}$ are largely an amplified version of the changes in $1\%_{21-70} - \text{PI}$, yet
 438 the resemblance between $1\%_{21-70} - \text{PI}$ and $H_{L50} - \text{PI}$ is limited.

439 There is a tendency for relatively stronger changes at higher latitudes than low latitudes
 440 in ω_Z for $H_{L50} - \text{PI}$, whereas the other two formulations have more evenly distributed

441 magnitudes of changes around the globe. Specifically, ω changes have similar patterns between
 442 the tunable Budyko formulation and the Fu formulation, but the Budyko formulation without the
 443 E/P constraint differs in many areas. Recalling that an increase in ω connotes a relationship
 444 between E/P and $R_{net}/\lambda P$ hews closer to the energy limits for all three formulations, the
 445 relationship moves closer to the water limit incidentally for ω_Z only where $\omega_Z \lesssim 1$. For $\omega_Z > 1$
 446 the moisture constraint is neglected. Thus, we see an increase in ω_Z over much of the eastern US
 447 for $H_{L50} - PI$ but decreases in ω_B and ω_F . If we look instead at the significance in the agreement
 448 among models (Figure 9), the discrepancies do not look as stark. Where signs of changes for ω_Z
 449 disagree with the other formulations, typically one or the other formulation is not significant. The
 450 three formulations agree most for the $1\%_{91-140} - 1\%_{21-70}$ changes, which also have the strongest
 451 and most widespread significant shifts in ω . For $H_{L50} - PI$ and $1\%_{21-70} - PI$ there is strong
 452 resemblance between patterns for ω_B and ω_F , while ω_Z has clear differences concentrated in
 453 more humid regions of the globe.

454 5 Interpretation of the Role of Vegetation

455 As noted earlier, the historical experiment contains many more specified climate drivers
 456 than the DECK experiments. As a result, we see changes from PI to H_{L50} differ from those in PI
 457 to $1\%_{21-70}$ in many locations (Figures 4, 5, 8 and 9). Clearly the other forcings are exerting more
 458 impact on hydroclimate than are greenhouse gas changes. Disentangling the specific drivers of
 459 hydroclimatic shifts in CMIP6 simulations is beyond the scope of this study. There are model
 460 intercomparison projects that investigate such impacts in more detail; those relevant to
 461 hydroclimate namely involve land use change (LUMIP; Lawrence et al. 2016) and soil moisture
 462 variations (LS3MIP; van den Hurk et al. 2016).

463 However, there is sufficient information to sort most models based on how they simulate
 464 vegetation. Some portion of the changes seen in the historical experiment come from progressive
 465 land use change. In the DECK experiments, the only specified evolving boundary condition is
 466 atmospheric CO_2 concentration, but other components of the Earth system can evolve in
 467 response including, if a model's land surface scheme allows it, vegetation.

468 The CMIP6 models fall into three distinct categories regarding vegetation modeling:
 469 those that include predicted phenology and dynamic vegetation (9 models); those that include
 470 only predicted phenology (13 models), and those that have neither (8 models). Specific model
 471 information is included in Table S1 in the supplementary material, including a fourth category
 472 excluded from this part of the analysis: models for which this information could not be reliably
 473 determined from discovered published literature (7 models).

474 We group model results into the first three categories to isolate the hydroclimate
 475 responses to predicted phenology and dynamic vegetation. Studies have suggested vegetation
 476 variations can be an important determinant for changes in the Budyko parameter ω (Donohue et
 477 al., 2012; Ning et al., 2019; S. Zhang et al., 2016, 2018). Changes in hydroclimate can be
 478 expressed in Budyko space in terms of variations or trends in aridity and E ratio relative to the
 479 Budyko curve (Jiang et al., 2015; D. Wang & Hejazi, 2011). Specifically, changes can be
 480 visualized as having two perpendicular axes – one parallel to the Budyko curve, and one
 481 perpendicular to it (D. Yang et al., 2009). Variations along the first axis imply that the curve
 482 itself is unchanging over time (i.e., the estimated value of ω is fairly constant) and any trends in
 483 the distribution of aridity and E ratio amount to a translation along the curve. Changes
 484 perpendicular to the Budyko curve imply the value of ω is changing. Figure 10 illustrates such

485 changes schematically, keeping in mind that there is not perfect consistency between changes in
 486 multi-model median ω (shifts in Budyko curves) and changes in multi-model median aridity and
 487 E ratio (Figure S5).

488 Yang et al. (2009) have suggested that movement along the Budyko curve represents
 489 changes in the climate but not in the landscape, whereas a shift normal to the Budyko curve
 490 indicates the natures of water storage, evapotranspiration and/or runoff have changed. For
 491 example, a shift in vegetation, changes in soil properties, active management of water resources
 492 or land use changes including agricultural expansion ought to alter the value of ω more than
 493 changes in mean temperature, humidity, precipitation or soil moisture. Thus, the role of
 494 vegetation in climate change ought to project predominantly on the perpendicular component.

495 To understand hydroclimatic changes in this context, we have taken the multi-model
 496 median values of aridity and E ratio at each grid cell for each CMIP6 experiment and the
 497 estimated values of ω_B , ω_F and ω_Z from their corresponding formulations, and decomposed the
 498 three temporal changes ($H_{L50} - PI$, $1\%_{21-70} - PI$, and $1\%_{91-140} - 1\%_{21-70}$) into changes parallel and
 499 perpendicular to the Budyko curve. The following process is used, also portrayed in Figure 10.
 500 First, because the median values of aridity and E ratio are not guaranteed to be a point that lies
 501 exactly on the best fit Budyko curve (Figure S5), the nearest point on the Budyko curve is found,
 502 and the slope of the Budyko curve at that point is used to establish a rotation of axes. For most
 503 points along the curves for all three formations, changes parallel to the curve correspond mainly
 504 to changes in aridity, increasingly so as aridity increases. However, for low aridity the slopes of
 505 the curves become steeper and the E ratio projects more strongly onto the axis parallel to the
 506 curve. For the Budyko formulation without the E/P constraint, as well as the variable exponent
 507 Budyko formulation when $\omega_B < 2$, the curves flatten out again at very low aridity (see Figure 1).

508 The rotated axes are translated so the origin is at the point of median aridity and E ratio
 509 for the earlier time period of each climate change comparison. The change in Budyko space to
 510 the new median for the later period is then reckoned as a distance parallel to the Budyko curve
 511 and a distance perpendicular to the curve. Figure S6 shows the ratio, parallel distance over
 512 perpendicular distance, for each formulation and the three change intervals. In each row, grid
 513 cells are only shown where the direct distance between the two median points is less than 2 times
 514 the standard error estimated from the multi-model median year-to-year variability during the
 515 earlier of the two periods. Masked out areas are considered not to be distinguishable from natural
 516 variability. Most changes are, in Budyko space, parallel to the estimated Budyko curve for the
 517 location. There is very little perceptible difference between maps for the different formulations.
 518 Overall, while shifts along the Budyko curve predominate, their relative magnitude tends to
 519 follow aridity itself, consistent with Figures 4 and 5. It is also apparent from the separate
 520 components (Figures S7 and S8) that movement along the Budyko curve, due to its overall
 521 positive slope, corresponds to synchronized increases or decreases in both aridity and E ratio.

522 Figure 11 shows how changes in ω_Z between the indicated pairs of experiments differ
 523 among models without predicted vegetation phenology or dynamic vegetation (left column), with
 524 predicted phenology but no dynamic vegetation (middle column) and with both dynamic
 525 vegetation and predicted phenology (right column). We use the significance in agreement among
 526 models projecting changes in ω_Z of the same sign to try to ameliorate the smaller sample sizes
 527 and the plethora of other differences between models.

528 There are significant regional changes of either sign as a result of both predicted
 529 phenology and DVMs, and there is more similarity in patterns within columns (i.e., in the
 530 evolution from PI to 1%₂₁₋₇₀ to 1%₉₁₋₁₄₀) than across columns. There appears to be a significant
 531 decrease in ω_Z over western Europe, coastal Australia, Mesoamerica, northern South America
 532 and much of southern Africa. Systematic increases are mainly confined to eastern Asia at middle
 533 and high latitudes. Broadly, models without any prognostic vegetation component (left column)
 534 show the weakest changes in ω_Z in most locations. Regions where changes are consistent in sign
 535 and significance across both time intervals are more likely to be genuine, but the global field
 536 significance (area of change of a particular sign and significance compared to what would be
 537 expected by random chance) is marginal, especially for decreases in ω_Z . Increases over many
 538 cold-winter regions are likely the signature of changes in annual snow cover affecting water
 539 storage – a process largely independent of vegetation.

540 The inclusion of predicted phenology in climate models appears to have a profound effect
 541 in the Amazon Basin, where models strongly agree on a decrease in ω_Z over a large area.
 542 Otherwise, there are many scattered locations of changes of both signs that cover much more
 543 area than in the left column. Addition of a DVM (right column) leads to additional significant
 544 (90% confidence or better) changes over about two-thirds of ice-free land, but no large areas of
 545 extremely high significance as seen in the middle column. This may reflect the less mature status
 546 of dynamic vegetation modeling compared to phenology modeling, and thus reduced consistency
 547 among the climate models including DVMs. Lastly, the tendency for changes in the 1%₉₁₋₁₄₀ –
 548 1%₂₁₋₇₀ case to be stronger than for 1%₂₁₋₇₀ – PI is weak in this analysis.

549 If changes in climate alone result in changes of aridity and E ratio that tend not alter ω , while landscape changes shift values of ω , there should be evidence by recalculating changes in
 550 Budyko space relative to axes parallel and perpendicular to the Budyko curve sorted by the
 551 sophistication of model vegetation parameterizations. Figures 12 and 13 show the ratio of
 552 changes (parallel over perpendicular) respectively comparing models with and without predicted
 553 phenology, and having predicted phenology but with and without DVMs. The right column of
 554 each figure shows the ratio of the ratios. Blue colors (ratios less than 1) indicate that shifts
 555 perpendicular to the Budyko curve, which result in changes in ω_Z , are larger than shifts along the
 556 curve. In the left two columns, which show the changes for the indicated subsets of models, the
 557 majority of significant changes are colored in shades of red, suggesting that overall, the shifts in
 558 hydroclimate are predominantly attributable to changing climate. However, we would expect
 559 more blue area in models with predicted phenology than without (Figure 12), and that is in fact
 560 evident in both time intervals. The histograms of the area in each ratio range help display this.
 561 Furthermore, the ratio of ratios (right column) tends to be predominantly blue: there is
 562 significantly more area < 1 than > 1. Similar results are seen for the effect of DVMs (Figure 13)
 563 although interestingly the tendency for hydroclimatological shifts perpendicular to the Budyko
 564 curve is not as strong as for the impact of predicted phenology. Nevertheless, the skewness in the
 565 histograms in the right column is also significant, suggesting DVMs also increase the likelihood
 566 of changes in ω_Z .

568 6 Conclusions

569 37 CMIP6 models have been examined regarding their portrayal of changes in
 570 hydroclimate, quantified via the Budyko framework that relates the partitioning of precipitation
 571 into evaporation at any location to that location's aridity. Alongside traditional formulations of

572 the Budyko equation, we have employed a new formulation that accounts for the fact that
573 frequently evaporation is not constrained by total precipitation on annual time scales due to
574 various terrestrial reservoirs of moisture (Figure 1). We have quantified the multi-model
575 climatology (Figures 2, 3, 6) and changes in aridity $R_{net}/(\lambda P)$, evaporation ratio (E/P) and the
576 parameter quantifying the local climatological relationship (ω) between the two across the
577 models for preindustrial, historical, and projected 1% per year increases in atmospheric CO₂
578 concentration, concentrating on multi-model medians and degree of model consensus (Figures 4,
579 5, 8, 9). The Budyko formulation without the E/P constraint provides the best fit to data over
580 more than half of the globe compared to two other common formulations (Figure 7).

581 We find that changes from preindustrial to recent historical (1965-2014) conditions are
582 often inconsistent with changes ascribable only to increasing CO₂. The historical simulations
583 include many other factors including atmospheric aerosols and land cover changes. We are able
584 to use model documentation to determine for most models whether or not they predict vegetation
585 phenology (rather than prescribe it as a boundary condition) and whether they employ dynamic
586 vegetation models (DVMs) that predict spatial changes in biomes in response to changing
587 climate. Theory suggests different meanings for changes in aridity and E ratio along the Budyko
588 curve than perpendicular to it, with perpendicular trends being ascribed to changes in landscape
589 (Figure 10).

590 There are clear differences in hydroclimate response depending on model treatment of
591 vegetation (Figure 11). CMIP6 models with predicted vegetation phenology consistently show
592 significantly larger changes in hydroclimate perpendicular to the Budyko curve, with a high
593 degree of inter-model consensus over large parts of the globe (Figure 12). The implication is that
594 models that do not predict phenology may be missing a key aspect of climate change. Models
595 containing DVMs also show widespread differences from those that do not, but the degree of
596 consensus among models is weaker (Figure 13). This may reflect the less mature state of these
597 models, which have not yet converged toward consistent and accurate representation of biome
598 responses to disturbance and climate change. Nevertheless, there is clear sensitivity that points to
599 the importance of representing biospheric shifts in Earth system models.

600 There are several caveats regarding the potential role of vegetation in this comparison.
 601 First, the treatment of vegetation is far from the only difference among these sets of models.
 602 However, it is unlikely that other parameterization differences would sort out exactly along the
 603 same lines as vegetation, so vegetation should contribute most of the signal determined. Second,
 604 the number of models in each category is different, so while variations in significance thresholds
 605 are accounted for, signal and noise in each set varies as well. Third, phenology and especially
 606 dynamic vegetation are not represented in the same way across models, so responses to climate
 607 change may not be consistent. This may account for more widespread but less consistent impact
 608 of the inclusion of DVMs on projected hydroclimate. Furthermore, we refrain here from
 609 validating any model or group of models as more accurate. There is a growing body of literature
 610 on ecological emergent constraints that provide convincing evidence for such vegetation-climate
 611 connections (Cox et al., 2013; Fisher et al., 2018; He et al., 2020; Lian et al., 2018; X. Wang et
 612 al., 2020; Wu et al., 2015). Nevertheless, we conclude that vegetation modeling is an important
 613 but possibly underappreciated aspect of climate change projections that can have important
 614 consequences for adaptation, especially regarding water resources and land management.

615 Acknowledgments, Samples, and Data

616 We thank the climate modeling groups cited in Tables 1 and S1 for making their model output
 617 available, the Earth System Grid Federation (ESGF) for archiving the data and providing access,
 618 and the funding agencies who have supported CMIP6 and ESGF. Data are available via the
 619 digital object identifiers listed in Table 1. We also acknowledge the World Climate Research
 620 Programme (WCRP) Working Group on Coupled Modelling (WGCM), which is responsible for
 621 CMIP6 coordination and promotion.

622 Data processing and preliminary analyses for this study were performed by the co-authors as part
 623 of a graduate class project in land-climate interactions in the Climate Dynamics Program of
 624 George Mason University, Fairfax, Virginia, USA. The lead author's synthesis of the student
 625 material was supported by funding from the National Science Foundation (AGS-1338427) for
 626 the Center for Ocean Land Atmosphere Studies (COLA).

628 References

- 629 Betts, A. K. (2004). Understanding Hydrometeorology Using Global Models. *Bulletin of the*
 630 *American Meteorological Society*, 85(11), 1673–1688. <https://doi.org/10.1175/BAMS-85-11-1673>
- 632 Brubaker, K. L., Entekhabi, D., & Eagleson, P. S. (1993). Estimation of Continental Precipitation
 633 Recycling. *Journal of Climate*, 6(6), 1077–1089. [https://doi.org/10.1175/1520-0442\(1993\)006<1077:EOCPR>2.0.CO;2](https://doi.org/10.1175/1520-0442(1993)006<1077:EOCPR>2.0.CO;2)
- 635 Budyko, M. I. (1974). *Climate and Life*. New York, NY, USA: Academic Press.
- 636 Burde, G. I., & Zangvil, A. (2001). The Estimation of Regional Precipitation Recycling. Part II:
 637 A New Recycling Model. *Journal of Climate*, 14(12), 2509–2527.
[https://doi.org/10.1175/1520-0442\(2001\)014<2509:TEORPR>2.0.CO;2](https://doi.org/10.1175/1520-0442(2001)014<2509:TEORPR>2.0.CO;2)
- 639 Carmona, A. M., Poveda, G., Sivapalan, M., Vallejo-Bernal, S. M., & Bustamante, E. (2016). A
 640 scaling approach to Budyko's framework and the complementary relationship of
 641 evapotranspiration in humid environments: case study of the Amazon River basin.

- 642 *Hydrology and Earth System Sciences*, 20(2), 589–603. <https://doi.org/10.5194/hess-20-589-2016>
- 643
- 644 Choudhury, BhaskarJ. (1999). Evaluation of an empirical equation for annual evaporation using
645 field observations and results from a biophysical model. *Journal of Hydrology*, 216(1),
646 99–110. [https://doi.org/10.1016/S0022-1694\(98\)00293-5](https://doi.org/10.1016/S0022-1694(98)00293-5)
- 647 Cox, P. M., Pearson, D., Booth, B. B., Friedlingstein, P., Huntingford, C., Jones, C. D., & Luke,
648 C. M. (2013). Sensitivity of tropical carbon to climate change constrained by carbon
649 dioxide variability. *Nature*, 494(7437), 341–344. <https://doi.org/10.1038/nature11882>
- 650 Destouni, G., Jaramillo, F., & Prieto, C. (2013). Hydroclimatic shifts driven by human water use
651 for food and energy production. *Nature Climate Change*, 3(3), 213–217.
652 <https://doi.org/10.1038/nclimate1719>
- 653 Dirmeyer, P. A., & Zeng, F. J. (1999). Precipitation Infiltration in the Simplified SiB Land
654 Surface Scheme. *Journal of the Meteorological Society of Japan. Ser. II*, 77(1B), 291–
655 303. https://doi.org/10.2151/jmsj1965.77.1B_291
- 656 Dirmeyer, P. A., Jin, Y., Singh, B., & Yan, X. (2013a). Evolving Land–Atmosphere Interactions
657 over North America from CMIP5 Simulations. *Journal of Climate*, 26(19), 7313–7327.
658 <https://doi.org/10.1175/JCLI-D-12-00454.1>
- 659 Dirmeyer, P. A., Jin, Y., Singh, B., & Yan, X. (2013b). Trends in Land–Atmosphere Interactions
660 from CMIP5 Simulations. *Journal of Hydrometeorology*, 14(3), 829–849.
661 <https://doi.org/10.1175/JHM-D-12-0107.1>
- 662 Donohue, R. J., Roderick, M. L., & McVicar, T. R. (2012). Roots, storms and soil pores:
663 Incorporating key ecohydrological processes into Budyko’s hydrological model. *Journal
664 of Hydrology*, 436–437, 35–50. <https://doi.org/10.1016/j.jhydrol.2012.02.033>
- 665 Eyring, V., Bony, S., Meehl, G. A., Senior, C. A., Stevens, B., Stouffer, R. J., & Taylor, K. E.
666 (2016). Overview of the Coupled Model Intercomparison Project Phase 6 (CMIP6)
667 experimental design and organization. *Geoscientific Model Development*, 9(5), 1937–
668 1958. <https://doi.org/10.5194/gmd-9-1937-2016>
- 669 Fisher, R. A., Koven, C. D., Anderegg, W. R. L., Christoffersen, B. O., Dietze, M. C., Farrior, C.
670 E., et al. (2018). Vegetation demographics in Earth System Models: A review of progress
671 and priorities. *Global Change Biology*, 24(1), 35–54. <https://doi.org/10.1111/gcb.13910>
- 672 Greve, P., Burek, P., & Wada, Y. (2020). Using the Budyko Framework for Calibrating a Global
673 Hydrological Model. *Water Resources Research*, 56(6), e2019WR026280.
674 <https://doi.org/10.1029/2019WR026280>
- 675 He, Y., Peng, S., Liu, Y., Li, X., Wang, K., Ciais, P., et al. (2020). Global vegetation biomass
676 production efficiency constrained by models and observations. *Global Change Biology*,
677 26(3), 1474–1484. <https://doi.org/10.1111/gcb.14816>
- 678 Hurk, B. van den, Kim, H., Krinner, G., Seneviratne, S. I., Derksen, C., Oki, T., et al. (2016).
679 LS3MIP (v1.0) contribution to CMIP6: the Land Surface, Snow and Soil moisture Model
680 Intercomparison Project – aims, setup and expected outcome. *Geoscientific Model
681 Development*, 9(8), 2809–2832. <https://doi.org/10.5194/gmd-9-2809-2016>

- 682 Jiang, C., Xiong, L., Wang, D., Liu, P., Guo, S., & Xu, C.-Y. (2015). Separating the impacts of
 683 climate change and human activities on runoff using the Budyko-type equations with
 684 time-varying parameters. *Journal of Hydrology*, 522, 326–338.
 685 <https://doi.org/10.1016/j.jhydrol.2014.12.060>
- 686 Koster, R. (2015). “Efficiency Space”: A Framework for Evaluating Joint Evaporation and
 687 Runoff Behavior*. *Bulletin of the American Meteorological Society*, 96(3), 393–396.
 688 <https://doi.org/10.1175/BAMS-D-14-00056.1>
- 689 Koster, R. D., & Suarez, M. J. (1999). A Simple Framework for Examining the Interannual
 690 Variability of Land Surface Moisture Fluxes. *Journal of Climate*, 12(7), 1911–1917.
 691 [https://doi.org/10.1175/1520-0442\(1999\)012<1911:ASFFET>2.0.CO;2](https://doi.org/10.1175/1520-0442(1999)012<1911:ASFFET>2.0.CO;2)
- 692 Kumar, S., Zwiers, F., Dirmeyer, P. A., Lawrence, D. M., Shrestha, R., & Werner, A. T. (2016).
 693 Terrestrial contribution to the heterogeneity in hydrological changes under global
 694 warming. *Water Resources Research*, 52(4), 3127–3142.
 695 <https://doi.org/10.1002/2016WR018607>
- 696 Lawrence, D. M., Hurtt, G. C., Arneth, A., Brovkin, V., Calvin, K. V., Jones, A. D., et al. (2016).
 697 The Land Use Model Intercomparison Project (LUMIP) contribution to CMIP6: rationale
 698 and experimental design. *Geoscientific Model Development*, 9(9), 2973–2998.
 699 <https://doi.org/10.5194/gmd-9-2973-2016>
- 700 Li, L., Wang, Y., Arora, V. K., Eamus, D., Shi, H., Li, J., et al. (2018). Evaluating Global Land
 701 Surface Models in CMIP5: Analysis of Ecosystem Water- and Light-Use Efficiencies and
 702 Rainfall Partitioning. *Journal of Climate*, 31(8), 2995–3008.
 703 <https://doi.org/10.1175/JCLI-D-16-0177.1>
- 704 Lian, X., Piao, S., Huntingford, C., Li, Y., Zeng, Z., Wang, X., et al. (2018). Partitioning global
 705 land evapotranspiration using CMIP5 models constrained by observations. *Nature
 706 Climate Change*, 8(7), 640–646. <https://doi.org/10.1038/s41558-018-0207-9>
- 707 Milly, P. C. D. (1994). Climate, soil water storage, and the average annual water balance. *Water
 708 Resources Research*, 30(7), 2143–2156. <https://doi.org/10.1029/94WR00586>
- 709 Milly, P. C. D., & Dunne, K. A. (2016). Potential evapotranspiration and continental drying.
 710 *Nature Climate Change*, 6(10), 946–949. <https://doi.org/10.1038/nclimate3046>
- 711 Milly, P. C. D., Betancourt, J., Falkenmark, M., Hirsch, R. M., Kundzewicz, Z. W., Lettenmaier,
 712 D. P., & Stouffer, R. J. (2008). Stationarity Is Dead: Whither Water Management?
 713 *Science*, 319(5863), 573–574. <https://doi.org/10.1126/science.1151915>
- 714 Milly, P. C. D., Betancourt, J., Falkenmark, M., Hirsch, R. M., Kundzewicz, Z. W., Lettenmaier,
 715 D. P., et al. (2015). On Critiques of “Stationarity is Dead: Whither Water Management?”
 716 *Water Resources Research*, 51(9), 7785–7789. <https://doi.org/10.1002/2015WR017408>
- 717 Miralles, D. G., Jiménez, C., Jung, M., Michel, D., Ershadi, A., McCabe, M. F., et al. (2016).
 718 The WACMOS-ET project – Part 2: Evaluation of global terrestrial evaporation data sets.
 719 *Hydrology and Earth System Sciences*, 20(2), 823–842. <https://doi.org/10.5194/hess-20-823-2016>
- 721 Ning, T., Zhou, S., Chang, F., Shen, H., Li, Z., & Liu, W. (2019). Interaction of vegetation,
 722 climate and topography on evapotranspiration modelling at different time scales within

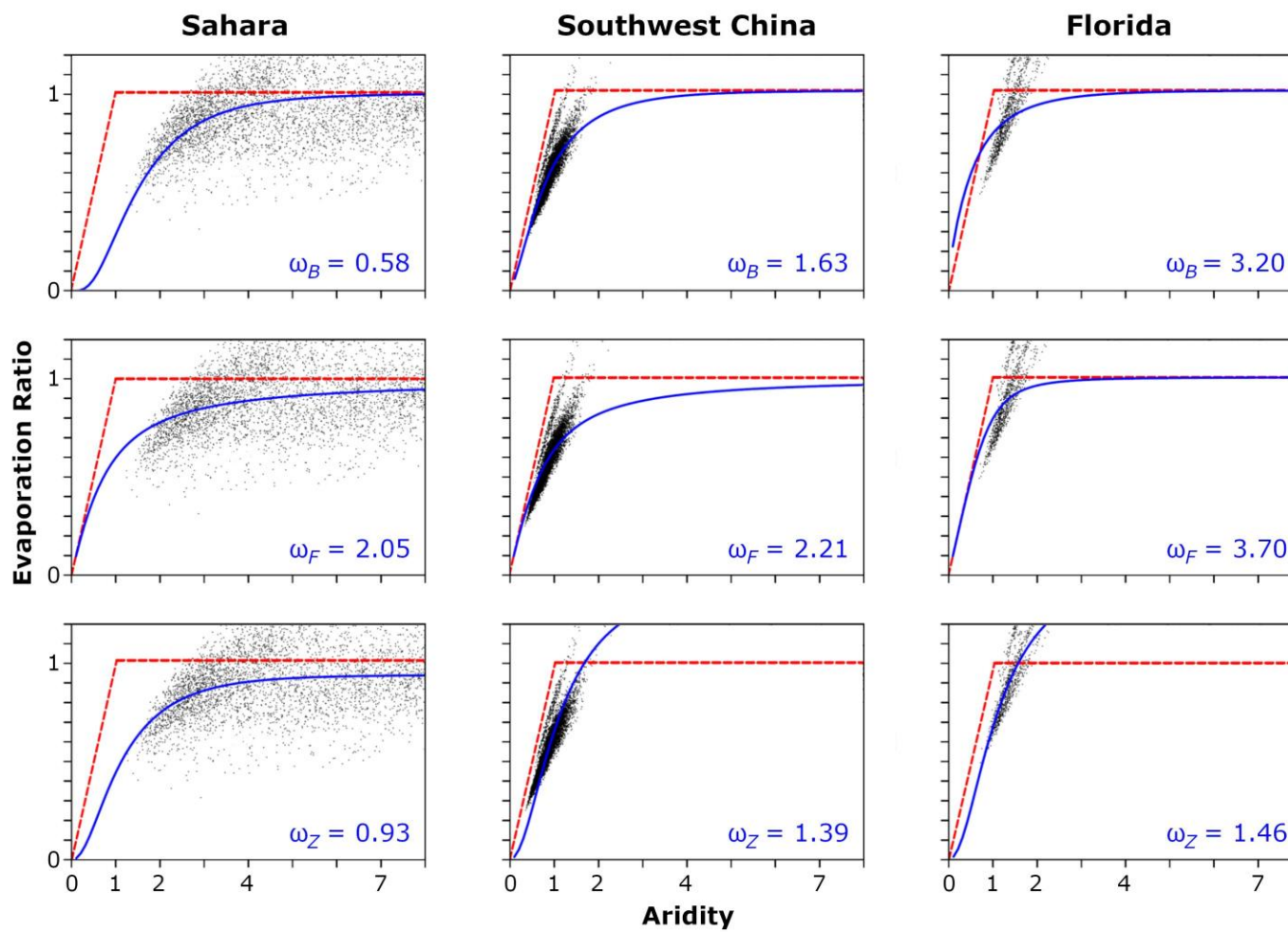
- 723 the Budyko framework. *Agricultural and Forest Meteorology*, 275, 59–68.
 724 <https://doi.org/10.1016/j.agrformet.2019.05.001>
- 725 Osborne, J. M., & Lambert, F. H. (2018). A simple tool for refining GCM water availability
 726 projections, applied to Chinese catchments. *Hydrology and Earth System Sciences*,
 727 22(11), 6043–6057. <https://doi.org/10.5194/hess-22-6043-2018>
- 728 Oudin, L., Andréassian, V., Lerat, J., & Michel, C. (2008). Has land cover a significant impact
 729 on mean annual streamflow? An international assessment using 1508 catchments.
 730 *Journal of Hydrology*, 357(3), 303–316. <https://doi.org/10.1016/j.jhydrol.2008.05.021>
- 731 Porada, P., Kleidon, A., & Schymanski, S. J. (2011). Entropy production of soil hydrological
 732 processes and its maximisation. *Earth System Dynamics*, 2(2), 179–190.
 733 <https://doi.org/10.5194/esd-2-179-2011>
- 734 Roderick, M. L., & Farquhar, G. D. (2011). A simple framework for relating variations in runoff
 735 to variations in climatic conditions and catchment properties. *Water Resources Research*,
 736 47(12). <https://doi.org/10.1029/2010WR009826>
- 737 Santanello, J. A., Dirmeyer, P. A., Ferguson, C. R., Findell, K. L., Tawfik, A. B., Berg, A., et al.
 738 (2018). Land-Atmosphere Interactions: The LoCo Perspective. *Bulletin of the American
 739 Meteorological Society*, 99, 1253–1272. <https://doi.org/10.1175/BAMS-D-17-0001.1>
- 740 Singh, R., & Kumar, R. (2015). Vulnerability of water availability in India due to climate
 741 change: A bottom-up probabilistic Budyko analysis. *Geophysical Research Letters*,
 742 42(22), 9799–9807. <https://doi.org/10.1002/2015GL066363>
- 743 Sposito, G. (2017). Understanding the Budyko Equation. *Water*, 9(4), 236.
 744 <https://doi.org/10.3390/w9040236>
- 745 Taylor, K. E., Stouffer, R. J., & Meehl, G. A. (2012). An Overview of CMIP5 and the
 746 Experiment Design. *Bulletin of the American Meteorological Society*, 93(4), 485–498.
 747 <https://doi.org/10.1175/BAMS-D-11-00094.1>
- 748 Wang, D., & Hejazi, M. (2011). Quantifying the relative contribution of the climate and direct
 749 human impacts on mean annual streamflow in the contiguous United States. *Water
 750 Resources Research*, 47(10). <https://doi.org/10.1029/2010WR010283>
- 751 Wang, D., & Tang, Y. (2014). A one-parameter Budyko model for water balance captures
 752 emergent behavior in darwinian hydrologic models. *Geophysical Research Letters*,
 753 41(13), 4569–4577. <https://doi.org/10.1002/2014GL060509>
- 754 Wang, X., Zhao, C., Müller, C., Wang, C., Ciais, P., Janssens, I., et al. (2020). Emergent
 755 constraint on crop yield response to warmer temperature from field experiments. *Nature
 756 Sustainability*, 3(11), 908–916. <https://doi.org/10.1038/s41893-020-0569-7>
- 757 Wu, D., Zhao, X., Liang, S., Zhou, T., Huang, K., Tang, B., & Zhao, W. (2015). Time-lag effects
 758 of global vegetation responses to climate change. *Global Change Biology*, 21(9), 3520–
 759 3531. <https://doi.org/10.1111/gcb.12945>
- 760 Xu, X., Liu, W., Scanlon, B. R., Zhang, L., & Pan, M. (2013). Local and global factors
 761 controlling water-energy balances within the Budyko framework. *Geophysical Research
 762 Letters*, 40(23), 6123–6129. <https://doi.org/10.1002/2013GL058324>

- 763 Yang, D., Shao, W., Yeh, P. J.-F., Yang, H., Kanae, S., & Oki, T. (2009). Impact of vegetation
764 coverage on regional water balance in the nonhumid regions of China. *Water Resources
765 Research*, 45(7). <https://doi.org/10.1029/2008WR006948>
- 766 Yang, Hanbo, & Yang, D. (2011). Derivation of climate elasticity of runoff to assess the effects
767 of climate change on annual runoff. *Water Resources Research*, 47(7).
768 <https://doi.org/10.1029/2010WR009287>
- 769 Yang, Hui, Piao, S., Huntingford, C., Ciais, P., Li, Y., Wang, T., et al. (2018). Changing the
770 retention properties of catchments and their influence on runoff under climate change.
771 *Environmental Research Letters*, 13(9), 094019. <https://doi.org/10.1088/1748-9326/aadd32>
- 773 Ye, S., Li, H.-Y., Li, S., Leung, L. R., Demissie, Y., Ran, Q., & Blöschl, G. (2015). Vegetation
774 regulation on streamflow intra-annual variability through adaption to climate variations.
775 *Geophysical Research Letters*, 42(23), 10,307-10,315.
776 <https://doi.org/10.1002/2015GL066396>
- 777 Zhang, L., Dawes, W. R., & Walker, G. R. (2001). Response of mean annual evapotranspiration
778 to vegetation changes at catchment scale. *Water Resources Research*, 37(3), 701–708.
779 <https://doi.org/10.1029/2000WR900325>
- 780 Zhang, L., Hickel, K., Dawes, W. R., Chiew, F. H. S., Western, A. W., & Briggs, P. R. (2004). A
781 rational function approach for estimating mean annual evapotranspiration. *Water
782 Resources Research*, 40(2). <https://doi.org/10.1029/2003WR002710>
- 783 Zhang, S., Yang, H., Yang, D., & Jayawardena, A. W. (2016). Quantifying the effect of
784 vegetation change on the regional water balance within the Budyko framework.
785 *Geophysical Research Letters*, 43(3), 1140–1148. <https://doi.org/10.1002/2015GL066952>
- 786 Zhang, S., Yang, Y., McVicar, T. R., & Yang, D. (2018). An Analytical Solution for the Impact
787 of Vegetation Changes on Hydrological Partitioning Within the Budyko Framework.
788 *Water Resources Research*, 54(1), 519–537. <https://doi.org/10.1002/2017WR022028>
- 789 Zheng, H., Chiew, F. H. S., Charles, S., & Podger, G. (2018). Future climate and runoff
790 projections across South Asia from CMIP5 global climate models and hydrological
791 modelling. *Journal of Hydrology: Regional Studies*, 18, 92–109.
792 <https://doi.org/10.1016/j.ejrh.2018.06.004>
- 793 Zhou, G., Wei, X., Chen, X., Zhou, P., Liu, X., Xiao, Y., et al. (2015). Global pattern for the
794 effect of climate and land cover on water yield. *Nature Communications*, 6(1), 5918.
795 <https://doi.org/10.1038/ncomms6918>
- 796

797 **Table 1.** List of CMIP6 models used. Full citations for each model are included in the
 798 supplement. “Grid” is for the atmospheric model component (horizontal cells: longitude x
 799 latitude).

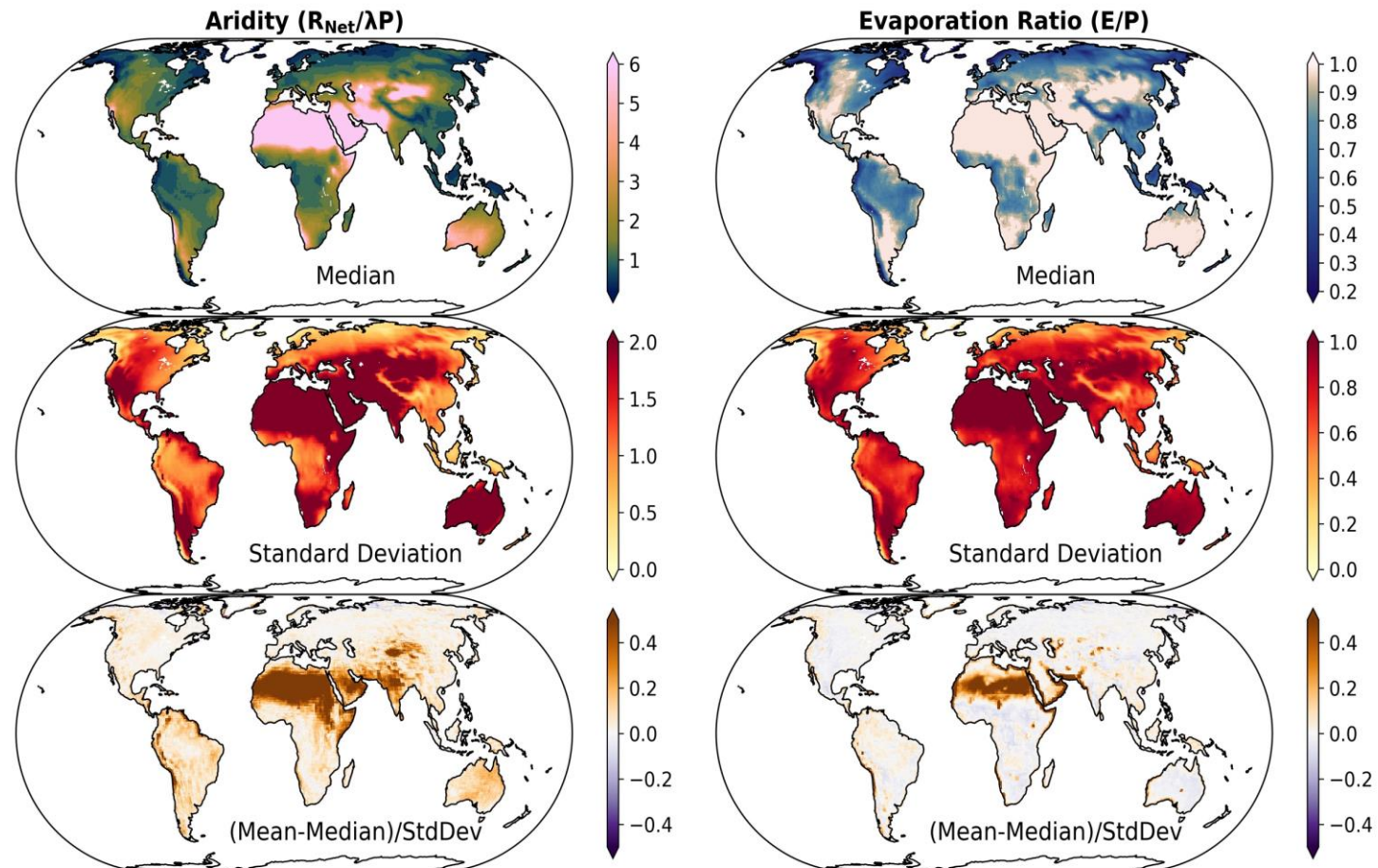
Institution	CMIP Label	Version	Variant	Grid	DOI
AWI	AWI-CM-1-1-MR	20191015	r1i1p1f1	384x192	10.22033/ESGF/CMIP6.359
BCC	BCC-CSM2-MR	20181015	r1i1p1f1	320x160	10.22033/ESGF/CMIP6.1725
BCC	BCC-ESM1	20190613	r1i1p1f1	128x64	10.22033/ESGF/CMIP6.1734
CAMS	CAMS-CSM1-0	20190708	r1i1p1f1	320x160	10.22033/ESGF/CMIP6.1399
CCCma	CanESM5	20190429	r1i1p1f1	128x64	10.22033/ESGF/CMIP6.1303
NCAR	CESM2	20190425	r1i1p1f1	288x192	10.22033/ESGF/CMIP6.2185
NCAR	CESM2-WACCM	20190425	r1i1p1f1	288x192	10.22033/ESGF/CMIP6.10024
NCAR	CESM2-WACCM-FV2	20200226	r1i1p1f1	144x96	10.22033/ESGF/CMIP6.11282
CNRM-CERFACS	CNRM-CM6-1	20180626	r1i1p1f2	256x128	10.22033/ESGF/CMIP6.1375
CNRM-CERFACS	CNRM-ESM2-1	20181018	r1i1p1f2	256x128	10.22033/ESGF/CMIP6.1391
E3SM-Project	E3SM-1-0	20190718	r1i1p1f1	360x180	10.22033/ESGF/CMIP6.2294
EC-Earth-Consortium	EC-Earth3	20200727	r1i1p1f1**	512x256	10.22033/ESGF/CMIP6.181
EC-Earth-Consortium	EC-Earth3-Veg	20200325	r1i1p1f1	512x256	10.22033/ESGF/CMIP6.642
CAS	FGOALS-g3	20191215	r1i1p1f1	180x80	10.22033/ESGF/CMIP6.1783
GFDL	GFDL-CM4	20180701	r1i1p1f1	288x180	10.22033/ESGF/CMIP6.1402
GFDL	GFDL-ESM4	20180701	r1i1p1f1	288x180	10.22033/ESGF/CMIP6.1407
NASA-GISS	GISS-E2-1-G	20180905	r1i1p1f1	144x90	10.22033/ESGF/CMIP6.1400
NASA-GISS	GISS-E2-1-H	20190403	r1i1p1f1	144x90	10.22033/ESGF/CMIP6.1421
MOHC	HadGEM3-GC31-LL	20190620	r1i1p1f3*	192x144	10.22033/ESGF/CMIP6.419
MOHC	HadGEM3-GC31-MM	20200115	r1i1p1f3*	432x324	10.22033/ESGF/CMIP6.420
INM	INM-CM4-8	20200226	r1i1p1f1	180x120	10.22033/ESGF/CMIP6.1422
INM	INM-CM5-0	20190530	r1i1p1f1	180x120	10.22033/ESGF/CMIP6.1423
IPSL	IPSL-CM6A-LR	20180727	r1i1p1f1	144x143	10.22033/ESGF/CMIP6.13581
NIMS-KMA	KACE-1-0-G	20190916	r1i1p1f1	192x144	10.22033/ESGF/CMIP6.2241
U. Arizona	MCM-UA-1-0	20190731	r1i1p1f1	96x80	10.22033/ESGF/CMIP6.2421
MIROC	MIROC-ES2L	20190823	r1i1p1f2	128x64	10.22033/ESGF/CMIP6.902
MIROC	MIROC6	20181212	r1i1p1f1	256x128	10.22033/ESGF/CMIP6.9121
HAMMOZ-Consortium	MPI-ESM-1-2-HAM	20190628	r1i1p1f1	192x96	10.22033/ESGF/CMIP6.1622
MPI-M DWD DKRZ	MPI-ESM1-2-HR	20190710	r1i1p1f1	384x192	10.22033/ESGF/CMIP6.741
MPI-M AWI	MPI-ESM1-2-LR	20190710	r1i1p1f1	192x96	10.22033/ESGF/CMIP6.742
MRI	MRI-ESM2-0	20190308	r1i1p1f1	320x160	10.22033/ESGF/CMIP6.621
NUIST	NESM3	20190707	r1i1p1f1	192x96	10.22033/ESGF/CMIP6.2021
NCC	NorCPM1	20190914	r1i1p1f1	144x96	10.22033/ESGF/CMIP6.10843
NCC	NorESM2-LM	20190815	r1i1p1f1	144x96	10.22033/ESGF/CMIP6.502
SNU	SAM0-UNICON	20190323	r1i1p1f1	288x192	10.22033/ESGF/CMIP6.1489
AS-RCEC	TaiESM1	20200225	r1i1p1f1	288x192	10.22033/ESGF/CMIP6.9684
MOHC NERC NIMS-KMA NIWA	UKESM1-0-LL	20190406	r1i1p1f2	192x144	10.22033/ESGF/CMIP6.1569

800 * piControl alone is r1i1p1f1 ** r3i1p1f1 for 1pctCO2 and r8i1p1f1 for 4xCO2



801
802
803
804
805
806
807

Figure 1. Comparison of the best fits (blue curves) through yearly data from a piControl simulation of a CMIP6 model at three different locations (labeled columns) for three formulations of the Budyko curve. Top row: Budyko formulation with tunable exponent; middle row: Fu (1981) formulation; bottom row: Budyko formulation without E/P constraint. Values of the single tunable exponent are shown in each panel, as are the theoretical energy and water limits (dashed red lines). Units of the axes are dimensionless.



808

809

810

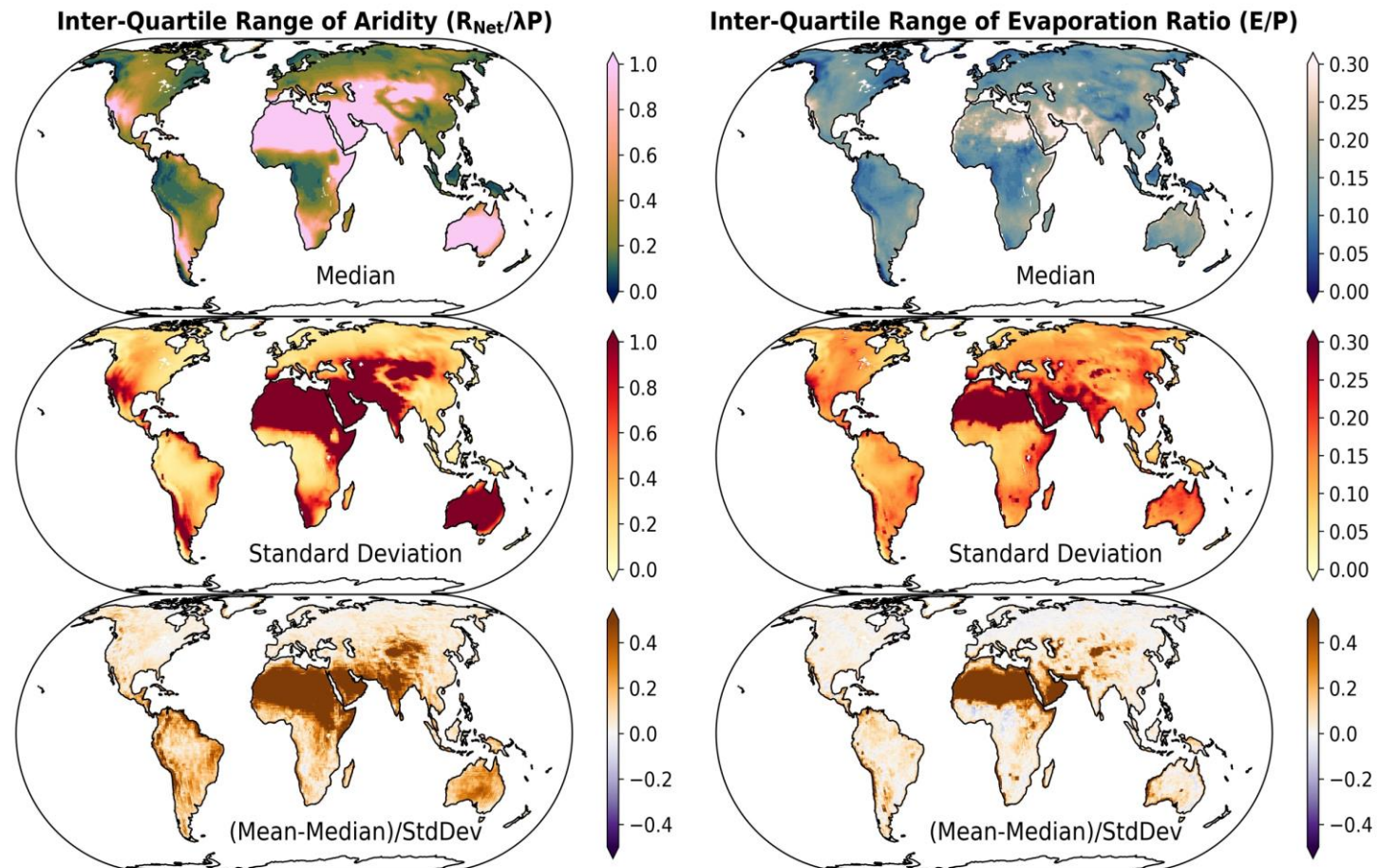
811

812

813

814

Figure 2. Multi-model statistics of aridity (left column) and E ratio (right column) calculated from each model's time-median from the piControl simulation. Top row: median at each location of individual model time-medians; middle row: standard deviation at each location of individual model time-medians; bottom row: The difference between the mean and median of individual model time-medians normalized by the standard deviation of individual model time-medians. All units are dimensionless.



815

816

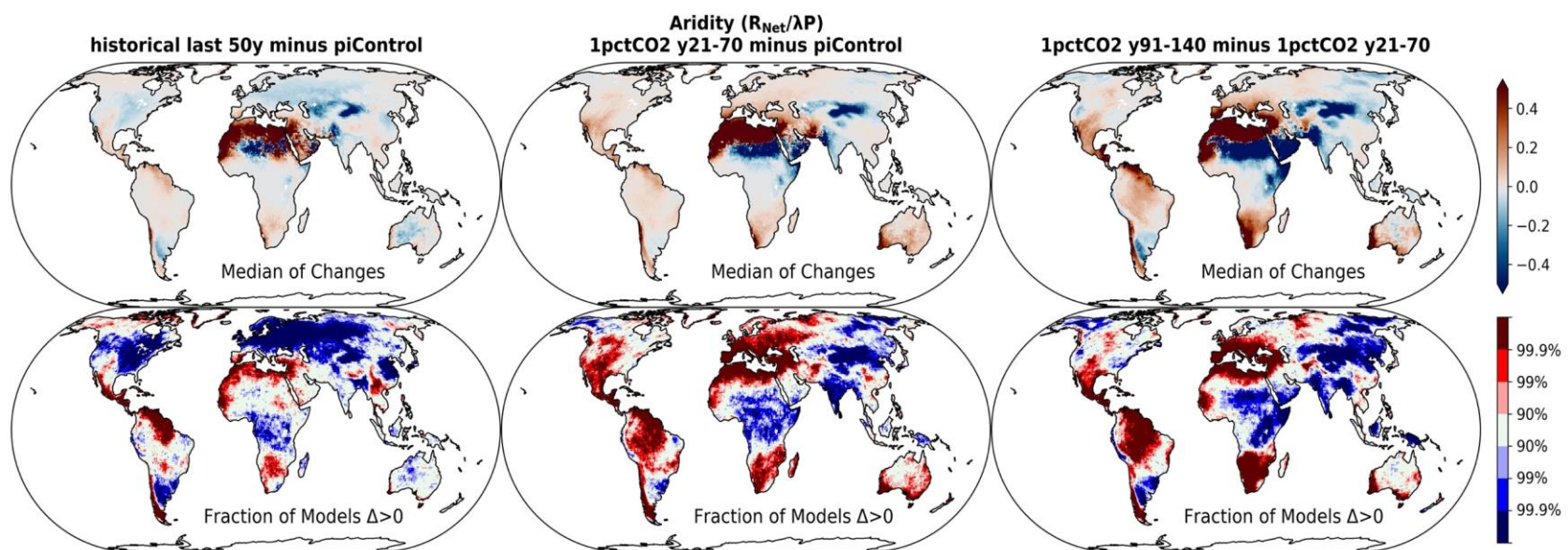
817

818

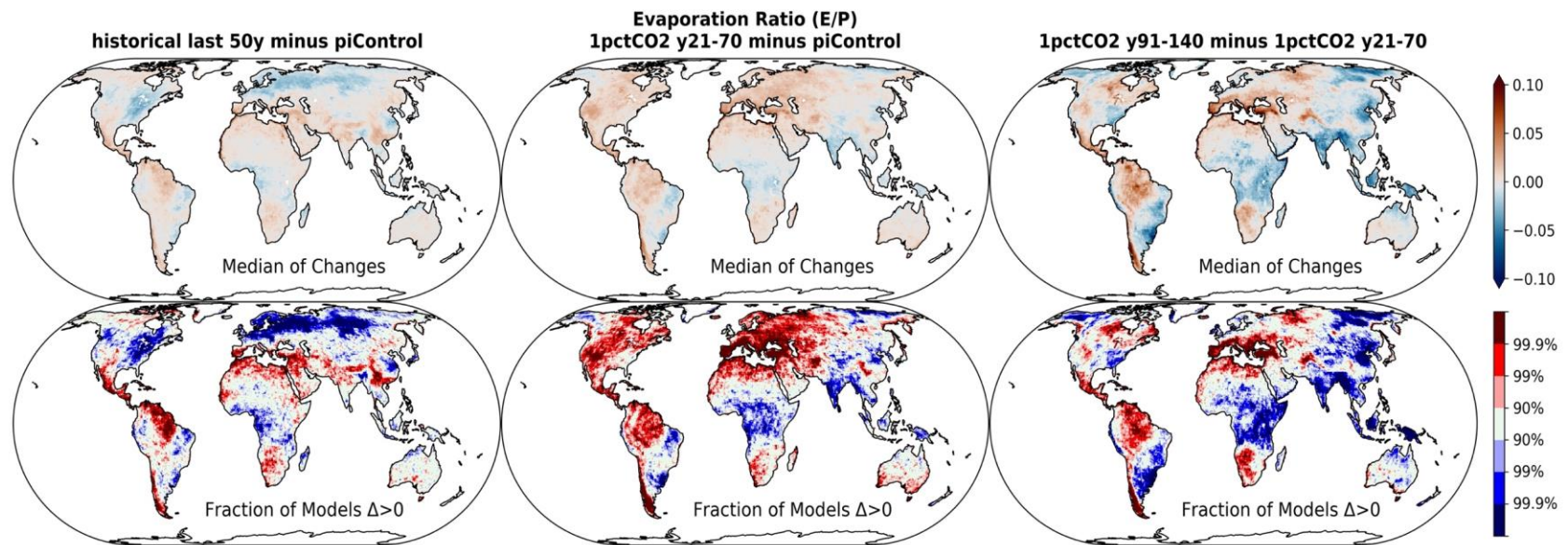
819

820

Figure 3. As in Figure 2 but applied to each model's inter-quartile ranges across all piControl years instead of each model's time medians.

821
822

823
824 **Figure 4.** Changes in aridity from PI to H_{L50} (left column); PI to $1\%_{21-70}$ (middle column); $1\%_{21-70}$ to $1\%_{91-140}$ (right column). The top
825 row shows the median change across all models at each location. The bottom row shows the significance of the fraction of models
826 agreeing on the sign of the change (red for positive change, blue for negative change).
827



828
829
830

Figure 5. As in Figure 4 for E ratio.

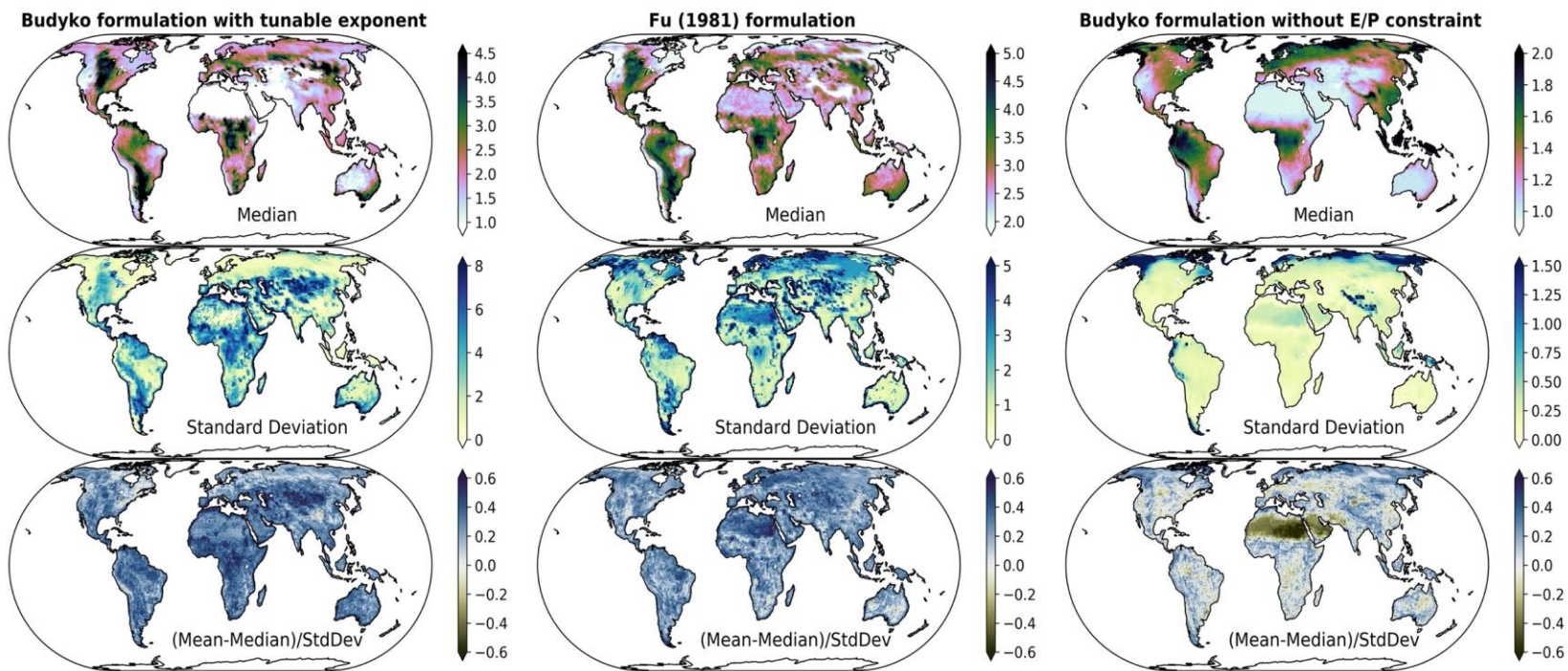
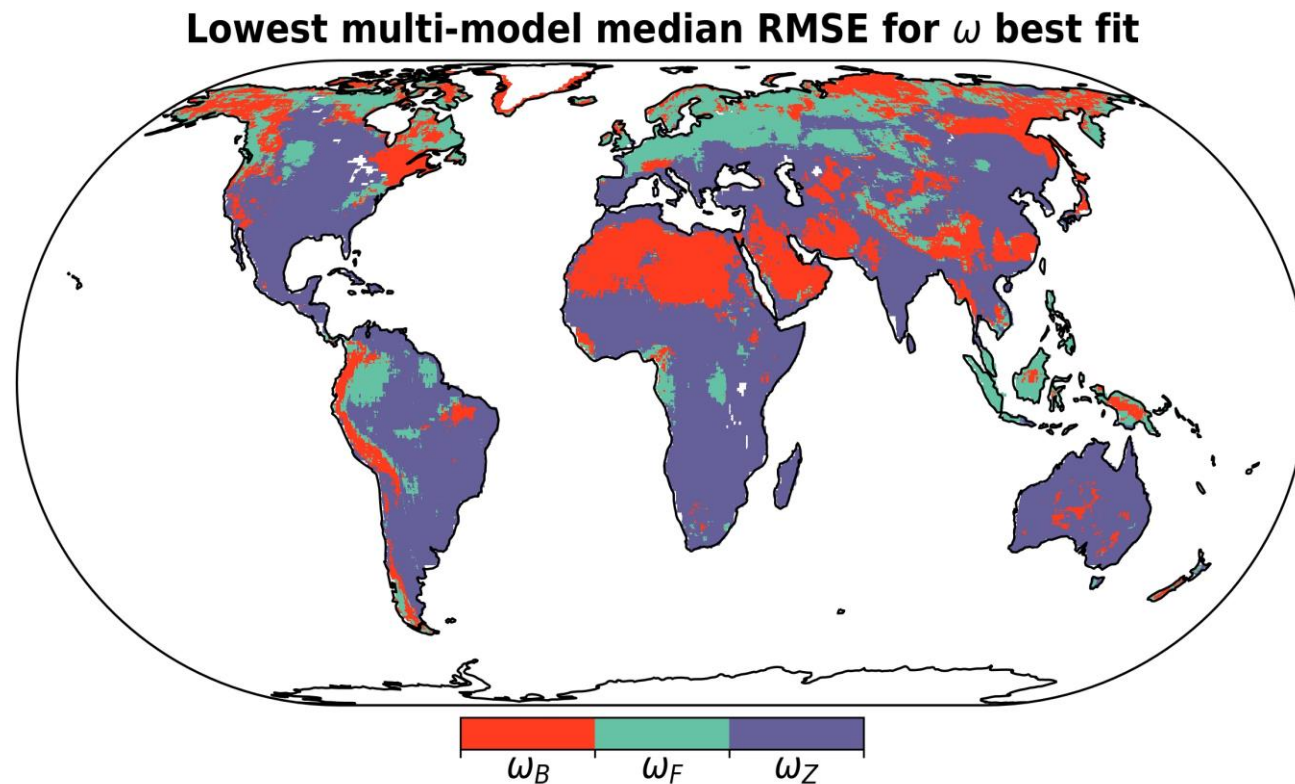
831
832
833
834
835
836

Figure 6. As in Figure 2 but for the single parameter of the indicated formulations: ω_B (left column); ω_F (middle column); ω_Z (right column).



837
838
839
840
841

Figure 7. Colors indicate which formulation of the Budyko curve best fits the distribution of annual values of E/P and $R_{net}/\lambda P$ across all models for the piControl experiment: ω_B indicates the Budyko formulation with the tunable exponent, ω_F is the Fu (1981) formulation, and ω_Z is the Budyko formulation without the E/P constraint.

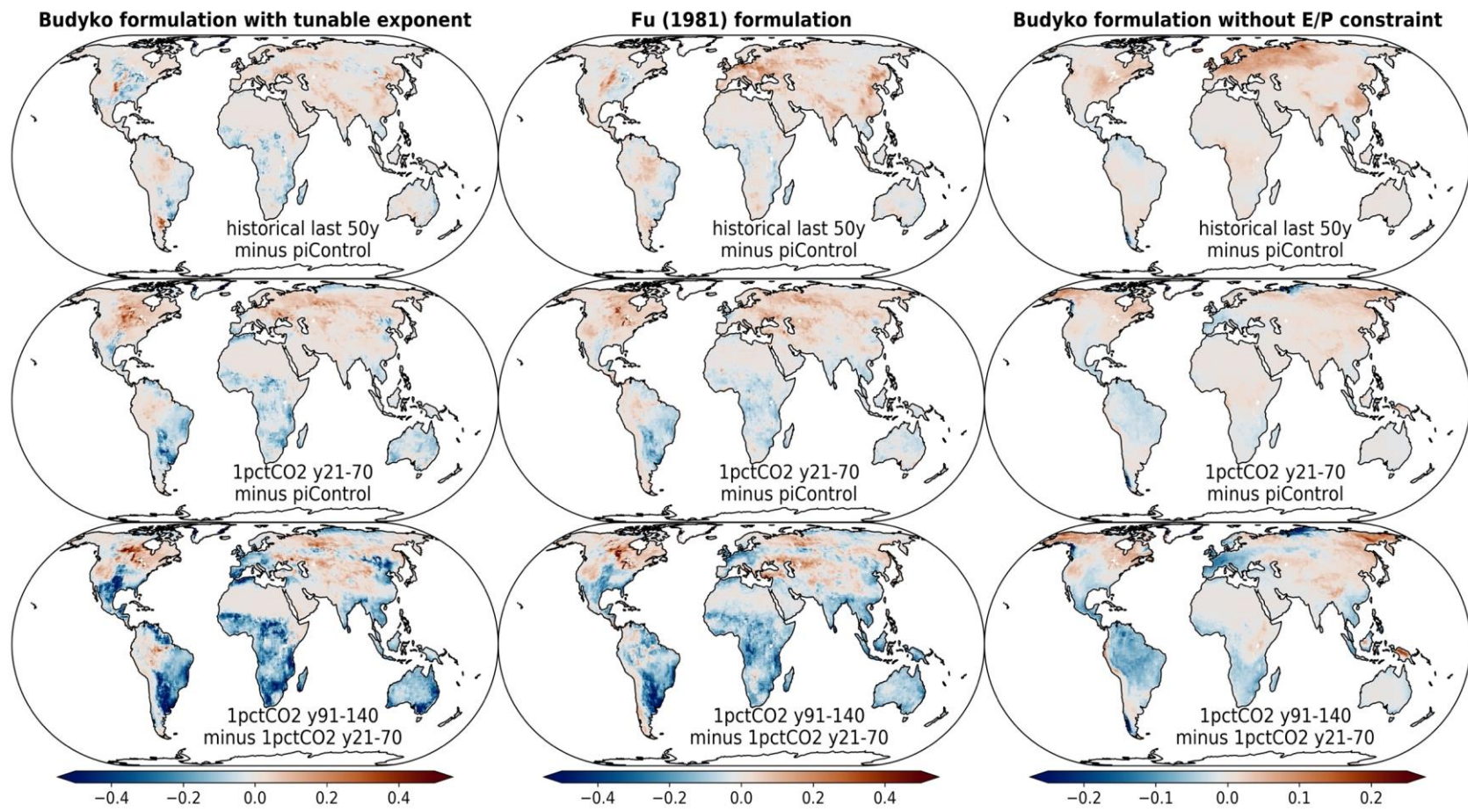
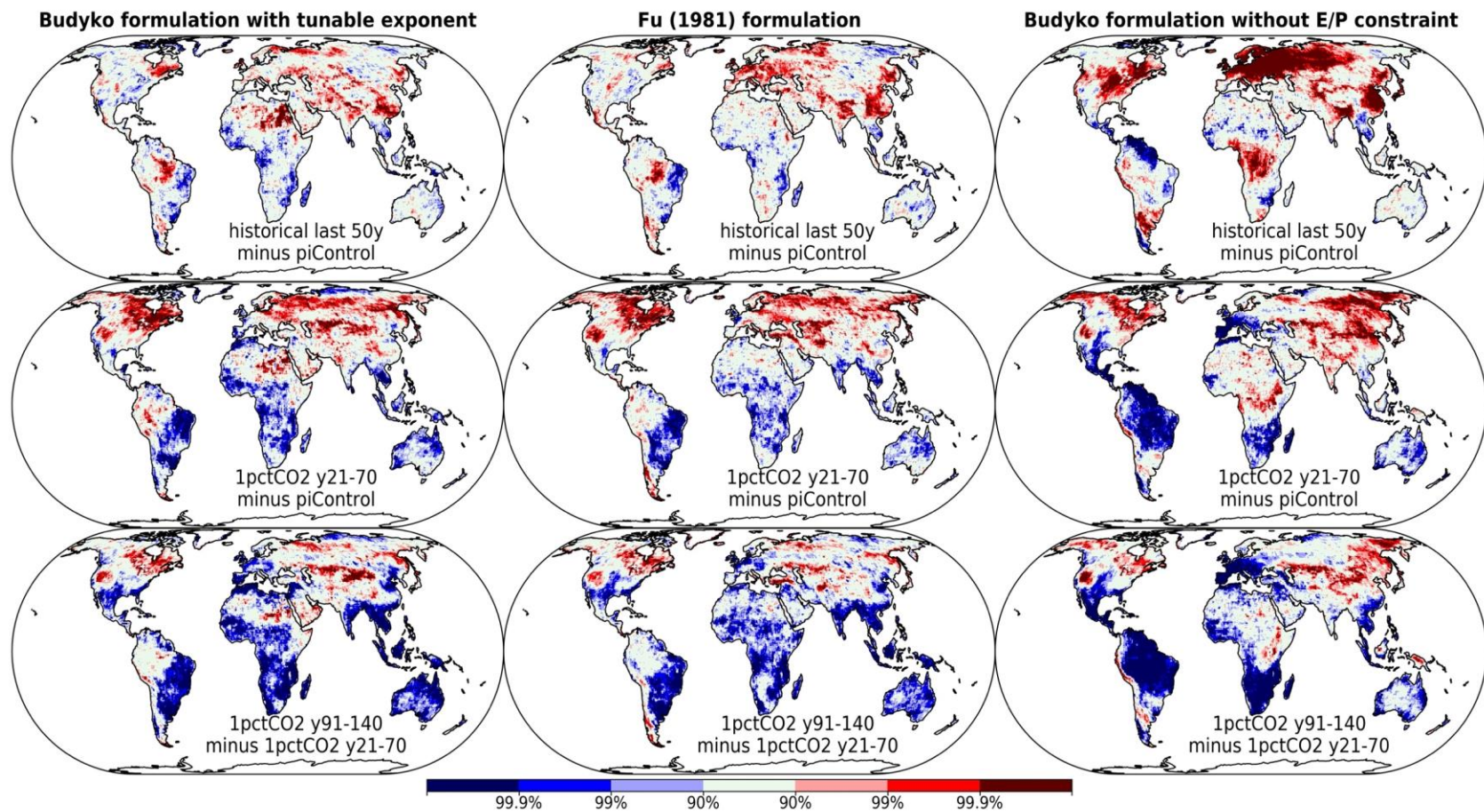
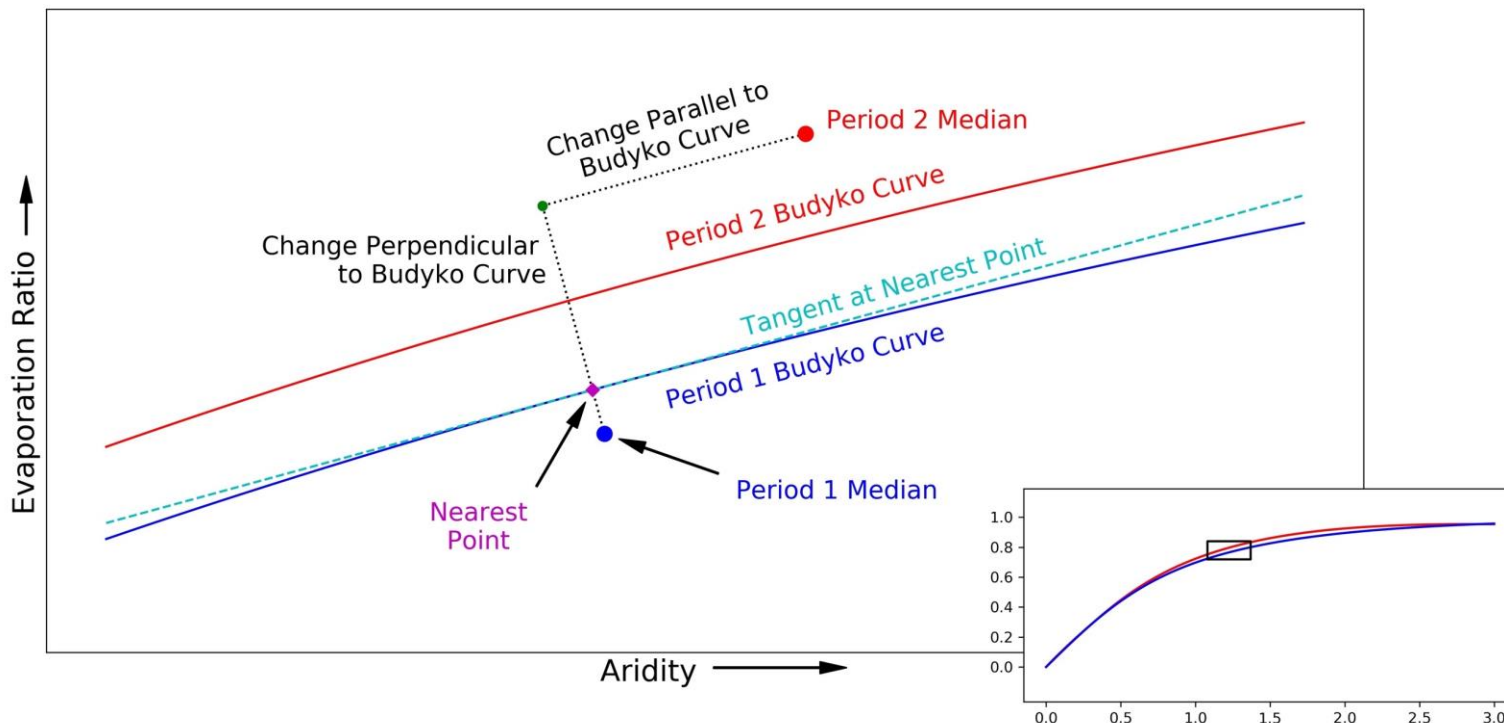
842
843
844
845
846
847

Figure 8. Changes from PI to H_{L50} (top row); PI to $1\%_{21-70}$ (middle row); $1\%_{21-70}$ to $1\%_{91-140}$ (bottom row) for the single parameter of the indicated formulations: ω_B (left column); ω_F (middle column); ω_Z (right column).

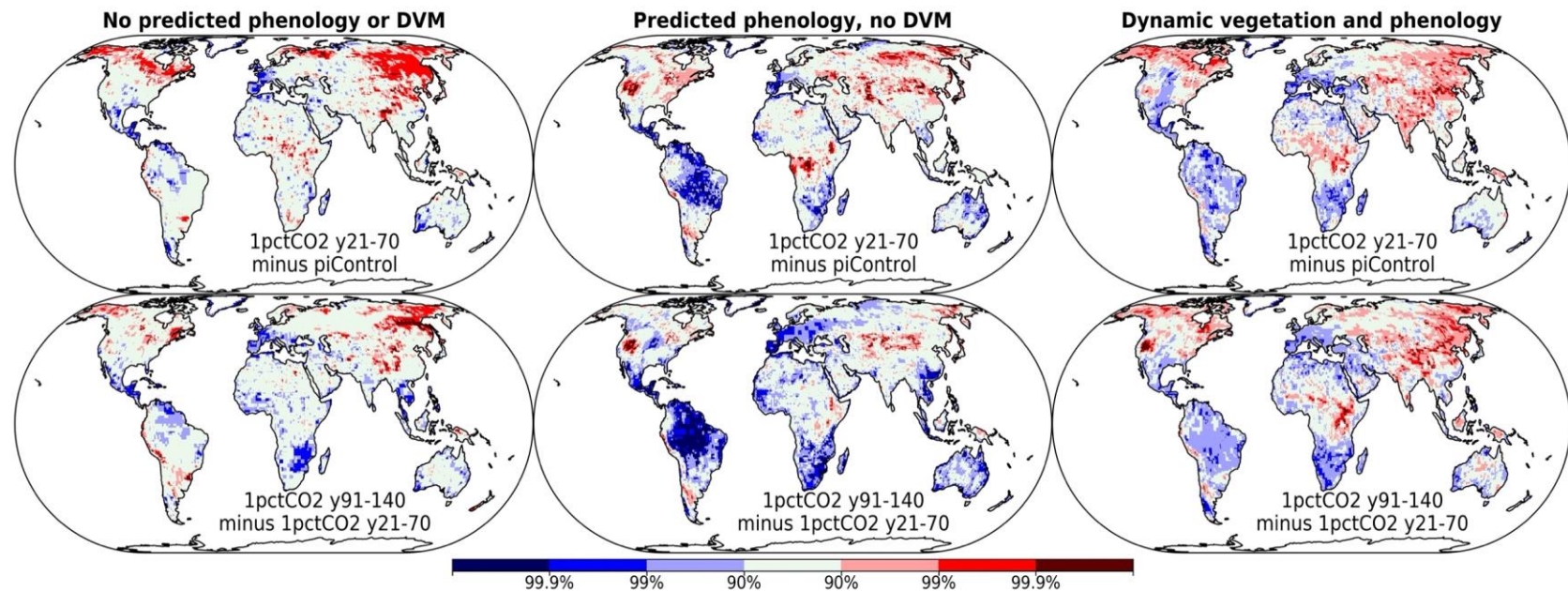


848
849
850
851
852

Figure 9. As in Figure 8 for the significance of the fraction of models agreeing on the sign of the change in ω (red for positive changes, blue for negative changes).

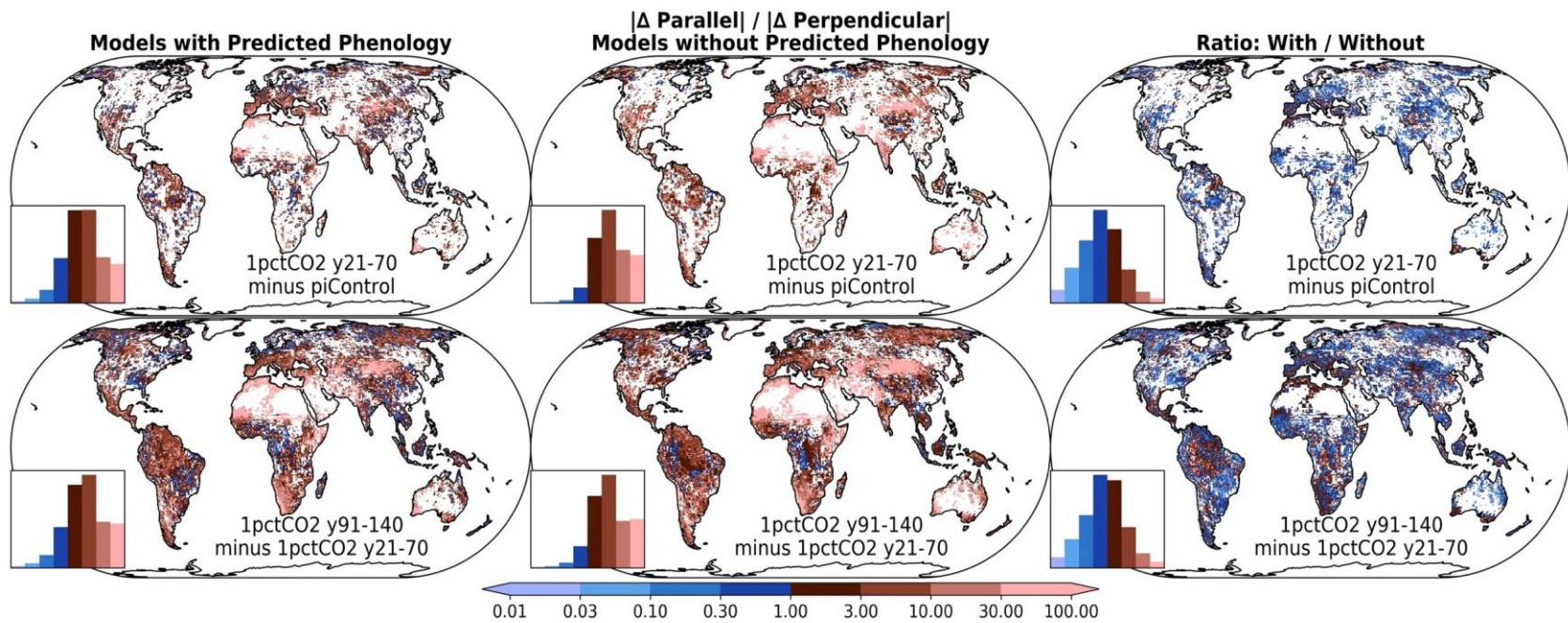


853
 854 **Figure 10.** Schematic showing two Budyko curves (blue and red)
 855 representing choices of ω that best fit the scatter of annual values of
 856 aridity and E ratio at a grid cell for two different periods in DECK simulations,
 857 or between PI and H_{L50} simulations. The main
 858 panel zooms in on the box indicated in the inset. The multi-model median values of aridity and E ratio for the different periods
 859 are shown by the large dots, and the best fit curves in their neighborhood are shown by solid lines of matching color. For the earlier
 860 period (Period 1 in blue), the nearest point on the Budyko curve to the median values is shown as a purple diamond. The slope of
 861 that curve is used to rotate the coordinate system to project the difference to median in the later period (Period 2 in red) into
 perpendicular and parallel components.



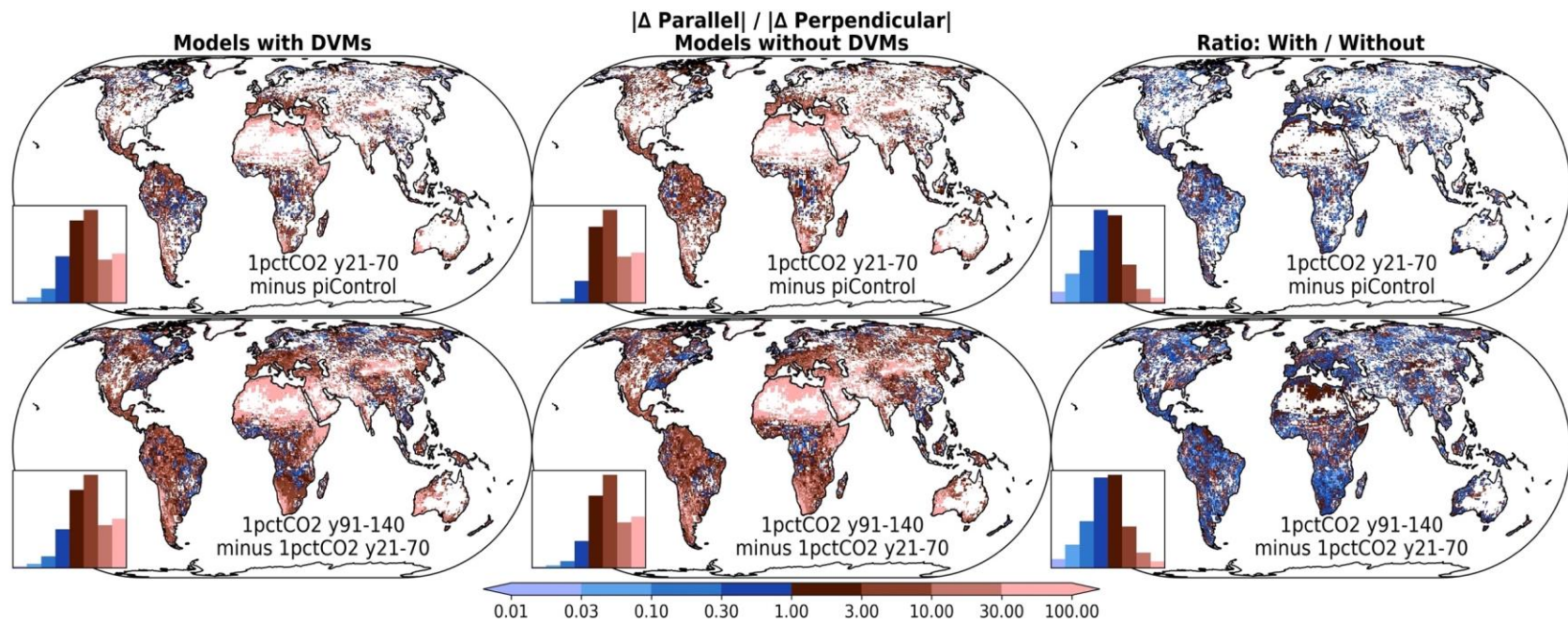
862
863
864
865
866

Figure 11. Significance of model agreement in the changes in ω_z from PI to 1%₂₁₋₇₀ (top row) and 1%₂₁₋₇₀ to 1%₉₁₋₁₄₀ (bottom row) only for models without predicted vegetation phenology or dynamic vegetation (left column), with predicted phenology but no dynamic vegetation (middle column) and with both dynamic vegetation and predicted phenology (right column).



867
868
869
870
871
872
873
874

Figure 12. The ratio of change parallel to the Budyko curve to change perpendicular to the Budyko curve from PI to 1%₂₁₋₇₀ (top row) and 1%₂₁₋₇₀ to 1%₉₁₋₁₄₀ (bottom row) only for models with predicted phenology but no dynamic vegetation (left column) without predicted phenology or dynamic vegetation (middle column) and the ratio of values from the left column over the middle column (right column). The inset histogram with each panel shows the proportion of ice-free land area in each color band, indicated by the color bar at the bottom of the figure.



875

876

877

878

879

Figure 13. As in Figure 12, except the left column is only for models with both predicted phenology and dynamic vegetation, and the middle column is only for models with predicted phenology but no dynamic vegetation.